Synergy between TROPOMI sun-induced chlorophyll fluorescence and MODIS spectral reflectance for understanding the dynamics of gross primary productivity at integrated carbon observatory system (ICOS) ecosystem flux sites

Hamadou Balde[1,2,3,4], Gabriel Hmimina[1], Yves Goulas[1], Gwendal Latouche[2], Kamel Soudani[2]

[1]Laboratoire de Météorologie Dynamique, Sorbonne Université, IPSL, CNRS/Ecole Polythétique, 91128, Palaiseau Cedex, France

[2]Ecologie Systématique et Evolution, Université Paris-Saclay, CNRS, AgroParisTech, 91190, Gif-sur-Yvette, France

[3]Centre national d'études spatiales (CNES), 18 av Edouard Belin, 31400 Toulouse.

[4]ACRI-ST, 260 Route du Pin Montard, BP 234, 06904 Sophia-Antipolis, France.

Correspondence to: Hamadou Balde (hamadou.balde@lmd.ispl.fr)

Abstract: An accurate estimation of vegetation Gross Primary Productivity (GPP), which is the amount of carbon taken up by vegetation through photosynthesis for a given time and area, is critical for understanding terrestrial-atmosphere CO_2 exchange processes, ecosystem functioning, and as well as ecosystem responses and adaptations to climate change. Prior studies, based on ground, airborne and satellite Sun-Induced chlorophyll Fluorescence (SIF) observations have recently revealed close relationships with GPP at different spatial and temporal scales and across different plant functional types (PFT). However, questions remain regarding whether there is a unique relationship between SIF and GPP across different sites and PFT and how can we improve GPP estimates using solely remotely sensed data. Using concurrent measurements of daily TROPOMI (TROPOspheric Monitoring Instrument) SIF (daily SIF_d), daily MODIS Terra and Aqua spectral reflectance, and vegetation indices (VIs, notably NDVI (normalized difference vegetation index), NIRv (near-infrared reflectance of vegetation) and PRI (photochemical reflectance index)) and daily tower-based GPP across eight major different PFT, including mixed forests, deciduous broadleaf forests, croplands, evergreen broadleaf forests, evergreen needleleaf forests, grasslands, open shrubland, and wetlands, the strength of the relationships between tower-based GPP and SIF_d at 40 ICOS (Integrated Carbon Observation Systems) flux sites was investigated. The synergy between SIF_d and MODIS based reflectance (R) and VIs to improve GPP estimates using a data-driven modelling approach was also evaluated. The results revealed that the strength of the hyperbolic relationship between GPP and SIF_d was strongly site-specific and PFT-dependent. Furthermore, the GLM (Generalized Linear Model) model, fitted between SIF_d, GPP, site and vegetation type as categorical variables, further supported this site-and PFT-dependent relationship between GPP and SIF_d. Using Random Forest Regression models (RF) with GPP as output and the aforementioned variables as predictors (R, SIFd and VIs), this study also showed that the spectral reflectance bands (RF-R), SIF_d plus spectral reflectance (RF-SIF-R) models explained over 80% of the seasonal and interannual variations in GPP, whereas the SIF_d plus VIs (RF-SIF-VI) model reproduced only 75% of the tower-based GPP variance. In addition, the relative variable importance of predictors of GPP demonstrated that the spectral reflectance bands in the near-infrared, red and SIF_d appeared as the most influential and dominant factors determining GPP predictions,

indicating the importance of canopy structure, biochemical properties and vegetation functioning on GPP estimates. Overall, this study provides insights into understanding the strength of the relationships between GPP

40   and SIF and the use of the spectral reflectance and SIF$_d$ to improve estimates GPP across sites and PFT.

1.   Introduction

In the context of climate change, understanding the role of terrestrial ecosystems in terms of exchanges of carbon, water and energy is crucial in order to fill-in the knowledge gap on climatic interactions between the biosphere and the atmosphere. Terrestrial ecosystems are one of the main components of the carbon cycle and are highly

45   sensitive to abiotic stresses. Therefore, an accurate estimation of vegetation Gross Primary Productivity (GPP), which is the carbon flux taken up by vegetation through photosynthesis, is critical for understanding terrestrial-atmosphere CO_2 exchange processes, ecosystem functioning, as well as ecosystem responses and adaptations to climate change (Gamon et al., 2019). Eddy Covariance (EC) techniques allow the estimation of GPP locally (Falge et al., 2002; Moureaux et al., 2008; Chu et al., 2021). However, they have limitations when it comes to upscale

50   carbon fluxes estimates at larger scales due to their restricted spatial coverage, temporal dynamics of flux footprints, and limited distribution across different vegetation types, notably in key areas such as Africa and South America (X. Xiao, 2004; Gamon, 2015; J. Xiao et al., 2019). GPP can also be estimated based on physical and ecophysiological modelling approaches. However, for estimating GPP at larger scales, those methods are hampered by the lack of understanding of the underlying physiological processes (Jiang & Ryu, 2016; Y. Zhang

55   et al., 2017; Madani et al., 2020).

Remote sensing is widely used to upscale daily GPP to landscape, regional, and global scales using reflected sunlight measured by satellite sensors (Running et al., 2004; Baldocchi et al., 2020 ; Wu et al., 2020 ; Kong et al., 2022; X. Wang et al., 2022). These approaches are mainly based on reflectance-based vegetation indices (VIs) such as Normalized Difference Vegetation Index (NDVI), Enhanced Vegetation Index (EVI) and more recently

60   near-infrared reflectance of vegetation (NIRv) (Badgley et al., 2017; Baldocchi et al., 2020). VIs are mostly sensitive to spatial and temporal variability in structural Leaf Area Index (LAI) and biochemical canopy attributes (Dechant et al., 2020; Pabon-Moreno et al., 2022), but they suffer from saturation in canopy dense ecosystems and are less sensitive to diurnal and daily variations in photosynthetic status resulting from physiological responses induced by rapid changes of abiotic stresses (Daumard et al., 2012; Guanter et al., 2014; Wieneke et al., 2016; Y.

65   Zhang, Zhang, et al., 2021). Remote sensing also provides access to variables which are related to canopy functioning such as the photochemical reflectance index (PRI) (Gamon et al., 1992; X. Wang et al., 2020) and Sun-Induced chlorophyll Fluorescence (SIF) (Porcar-Castell et al., 2014; Goulas et al., 2017; Magney et al., 2019; P. Yang et al., 2020; J. Zhang et al., 2022; X. Li & Xiao, 2022).

PRI is a reflectance-based vegetation index, that has been shown to detect vegetation functioning activities under

70   abiotic stress conditions that above-mentioned VIs cannot capture (Meroni et al., 2008). It is due to changes in the absorptance of leaves around 510 nm or reflectance at 531 nm that are related to the interconversion of the xanthophyll pigment cycles, which represents an important photoprotection mechanism (Gamon et al., 1992; Meroni et al., 2008). Moreover, previous studies pointed out that PRI can be used to improve canopy GPP estimates at the ecosystem level at daily timescale (X. Wang et al., 2020; Hmimina et al., 2015; Soudani et al., 2014), but

75   how variations in PRI at long timescales with spatial variations of vegetation types affect the relationship between

PRI and GPP remains unresolved and an area of active research (Porcar-Castell et al., 2014; Chou et al., 2017; Gitelson et al., 2017).

In recent years, SIF has emerged as a promising remotely sensed tool for monitoring canopy GPP, which is functionally and fundamentally different from the aforementioned VIs (Damm et al., 2010; X. Yang et al., 2015; Köhler et al., 2018; N. Wang et al., 2021; Guanter et al., 2021). In fact, SIF does not rely on vegetation reflectance, instead it is a faint signal directly emitted by chlorophyll from the absorbed sunlight just before the occurrence of photochemical reaction (Porcar-Castell et al., 2014; Gu et al., 2019; Zhang et al., 2021). SIF has a physical and physiological meanings, and hence SIF offers new opportunities for global assessment of canopy GPP (Mohammed et al., 2019; Wieneke et al., 2018; Zhang et al., 2020; Kimm et al., 2021; Dechant et al., 2022). Earlier studies relying on ground-based, airborne and satellite SIF data measurements at different temporal and spatial scales have indicated a strong linear site-specific and vegetation types dependent relationship between GPP and SIF (Frankenberg et al., 2011; Guanter et al., 2014; Yang et al., 2017; Wood et al., 2017; Li et al., 2018; Paul-Limoges et al., 2018; Zhang et al., 2021; Zhang et al., 2022). In contrast, at finer temporal scales such as diurnal and hourly, the relationship between GPP and SIF is not as strong as at longer timescales. Instead, it appears to be non-linear due to rapid changes in instantaneous variations in PAR and environmental conditions (Damm et al., 2015; Marrs et al., 2020; Kim et al., 2021). How and at which extent driving factors such as canopy structure, spatial heterogeneity and abiotic stress conditions mediate the GPP and SIF relationship remains a challenge and needs to be investigated (Smith et al., 2018; Wang et al., 2021; Li & Xiao, 2022). The main drawback relates to the use of SIF to predict GPP at regional and global scales lies on the difficulties in the weak SIF signals retrieval requiring averaging over large time and spatial scales, and thus hampers detecting fine-scale dynamics needed to explain underlying processes (Gamon et al., 2019; Köhler et al., 2021).Yet, the TROPOspheric Monitoring Instrument (TROPOMI) sensor, which is on board Sentinel 5-Precursor, represents a novel tool for understanding SIF variations as well as an opportunity to fully evaluate the potential of SIF to improve GPP estimates at the ecosystem scale as it provides a high temporal resolution at daily scale (Köhler et al., 2018). In addition, the future satellite mission FLEX (Fluorescence Explorer) will provide on a single platform SIF at an unprecedented spatial resolution (300m) together with visible reflectance in the green, red and far red spectral windows (Drusch et al., 2017).

The surface spectral reflectance (R), VIs and SIF can be used altogether to better characterize highly spatiotemporal dynamics in vegetation canopy structure, canopy biochemical properties and vegetation functioning as a response to frequent changes in abiotic conditions at the site and ecosystem scales. However, to the best of our knowledge, an attempt to study the synergy between those variables have not been comprehensively addressed due to the fact that the relationships between structural and functional components are not linear, and have complex interactions over time and space (Hilker et al., 2007; Sippel et al., 2018; Yazbeck et al., 2021; Pabon-Moreno et al., 2022; Kong et al., 2022). Therefore, a series of observations of SIF, R and VIs at the site et ecosystem scales could give insights about how SIF is related to GPP, and whether SIF and R, and VIs would provide additional information on understanding the dynamics of GPP at the ecosystem scale and beyond.

The overarching objective of this work is to study the potential of SIF, R and VIs (namely NDVI, NIRv, and PRI) to estimate canopy GPP, and the synergy between these predictive variables. Specifically, this study primarily intends to evaluate at daily timescale the strength of the relationships between SIF and GPP at 40 ICOS flux sites, including several vegetation functional types (mixed forests, deciduous broadleaf forests, croplands, evergreen

broadleaf forests, evergreen needleleaf forests, grasslands, open shrubland, and wetland), and ultimately to examine the synergy between SIF, R and VIs to improve canopy GPP estimates based on data-driven modelling approach.

2.   Materials and Methods

120   In this current section, the site characteristics and Eddy Covariance (EC) flux data are presented. Then, the remote sensing data (TROPOMI, MODIS Aqua and Terra, and Copernicus Land Cover classification) used in the study are described. At last, data analysis methods used in this study are presented.

2.1   Study Sites and flux tower in-situ data

EC flux data were obtained through the Integrated Carbon Observation System (ICOS) data portal release 2018
125   and 2021 (https://www.icos-cp.eu/data-services). We screened over 70 ecosystem ICOS sites relying on the availability of GPP data for each site with simultaneous TROPOMI SIF observations in the period from February 2018 to December 2020, and maintained 40 sites for analyses. The study sites encompass from a latitude 5.27 °N to 67.75 °N, including a diversity of plant functional types (PFT) based on the IGBP vegetation types classification given by ICOS PI sites: Mixed Forests (MF, 2 sites), Croplands (CRO, 9 sites), Deciduous Broadleaf Forests (DBF,
130   6 sites), Evergreen Broadleaf Forest (EBF, 2 sites), Evergreen Needleleaf Forests (ENF, 13 sites), Grasslands (GRA, 3 sites), Open Shrubland (OSH, 1 site, which is actually a young vineyard plantation), and Wetlands (WET, 4 sites). The PFT at each site was confirmed by photointerpretation of pictures found in ICOS data portal database and Google Earth. Detailed information and references of these sites are provided in Supplementary Materials in Tab S1. Figure 1 presents the location of these study sites, except for GF-Guy site, located in French Guiana. In
135   the analyses, we used daily GPP values computed as the sum of the half-hourly values estimated from each site. GPP data previously gap filled by ICOS PI representing for a full year, which was the case for instance at *CH-Dav, FR-Bil, IT-SR2,* and *SE-Deg*, are filtered out and were not used in the analyses.
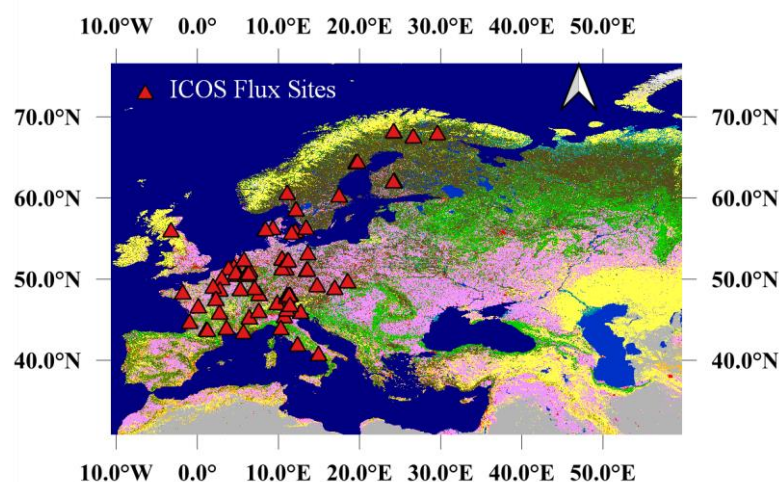
Figure 1: The study area and location of the EC ICOS flux sites, except for GF-Guy site, located in French Guiana. The base
140   map is the 100 m spatial resolution of the Copernicus Global Land Cover Classification map. The triangles represent the locations of the flux sites used for investigating the relationships between tower-based GPP and TROPOMI SIF.

2.2 Remote Sensing data

2.2.1 MODIS Terra and Aqua Data

Timeseries of daily MODIS Terra and Aqua surface reflectance products (MOD09GA, MODOCGA, MYD09GA and MYDOCGA), centered at the location of each site, were downloaded from Google Earth Engine database. The quality assurance (QA) flag (ideal quality, QA = 0) and the cloud mask (clear, cloud state = 0) criteria were used. Both MODIS Terra and Aqua, used in this study, contain 16 spectral bands of which, the spatial resolution from band 1 to band 7 is 500 m, and 1 km for the remaining bands (8-16) (Vermote et al., 2015). A detailed information about the MODIS data products is given in Supplementary Materials in Tab S2. We used daily MODIS surface reflectance, NDVI, NIRv, and PRI. These VIs are computed according the equation given in Table 1. For PRI computation, we used B_{13} as a reference band following (Hilker et al., 2009).

Table 1 : MODIS Terra and Aqua vegetation indices computations. B_2 (841-876 nm) denotes surface spectral reflectance at band 2, B_1 (620-670 nm) denotes surface spectral reflectance at band 1, B_{11} (526-536 nm) represents the surface spectral reflectance at band 11, and B_{13} (662-672 nm) represents the surface spectral reflectance at band 13.

Acronym	Full Name	Formulation	Spatial Resolution	References
NDVI	Normalized Difference Vegetation Index	$(B_2 - B_1)/(B_2 + B_1)$	500 m	(Tucker, 1979)
PRI	Photochimal Reflectance Index	$(B_{11} - B_{13})/(B_{11} + B_{13})$	1 km	(Drolet et al., 2008; Hilker et al., 2009)
NIRv	Near-Infrared Reflectance of Vegetation	$B_2 \times NDVI$	500 m	(Badgley et al., 2017)

2.2.2 TROPOMI SIF and Copernicus Global Land Cover data

TROPOMI, as a single payload of the Sentinel-5 Precursor (S-5P) satellite, was launched on October 13, 2017. TROPOMI has a near sun-synchronous orbit with a repeat cycle of 16 days and an equatorial crossing time at around 13:30 local time (Köhler et al., 2018), which is comparable to those of OCO-2 (Orbiting Carbon Observatory-2) and GOSAT (Greenhouse Gases Observing Satellite). However, the wide swath of TROPOMI (2600 km) is larger than that of OCO-2 (10 km), which enables TROPOMI to provide almost daily spatially continuous global coverage (Köhler et al., 2018). TROPOMI has a spatial resolution of 7 km along track (5 km since August 2019 owing to diminish integration time) and 3.5 to 14 km across track (based on the viewing angle) and covers the spectral range between 675-775 nm in the near infrared with a spectral resolution of 0.5 nm, which allows the retrieval of far-red SIF (Köhler et al., 2018). To decouple SIF emissions from the reflected incident sunlight, a statistical and data-driven approach is used, see Köhler et al. (2018) for more details. We used instantaneous and daily ungridded soundings of TROPOMI far-red SIF at 740 nm obtained from Caltech dataset between February, 2018 and December, 2020 (https://data.caltech.edu/records/1347). Instantaneous SIF data were reported in ($mW\ m^{-2}\ sr^{-1}\ nm^{-1}$). Daily SIF (hereafter referred as SIF_d) is computed by timing instantaneous SIF with a day length correction factor included in the dataset.

The TROPOMI SIF observations corresponding to each site were determined relying on the following criteria. Firstly, we extracted all pixels which center locations are less than 5 km away from the flux tower sites for analyses. The latter choice was motivated due to the fact that the relationship between TROPOMI SIF and tower-based GPP gradually weakened as the distance between sites to the center of pixels increased (data not shown). Secondly, to reduce the cloud effects on SIF data, SIF_d observations with cloud fraction over 15% were excluded, even though, some findings reveal that TROPOMI SIF is less sensitive to cloud than surface reflectance values (Guanter et al., 2012; Doughty et al., 2021). The 100 m spatial resolution of the Copernicus Global Land Cover Classification map for the year 2019 (Buchhorn et al., 2020) was used as a based map of the study sites. This land cover classification map was obtained from the Copernicus Global Land Service website (https://lcviewer.vito.be/download).

3.   Data Analysis

In this study, the GPP and SIF_d relationship was evaluated at the daily timescale at different spatial scales. Before investigating the link between GPP and SIF_d, it was necessary to figure out a way to process outliers which were mostly associated with negative SIF_d values. It has been shown that excluding directly negative SIF values could have effects on studying the relationships between satellite SIF data and GPP (Köhler et al., 2018; Köhler et al., 2021). Thus, to handle the outliers, an exponential model was used to account for the structural relationship between the instantaneous SIF and the SIF error included in the dataset. A threshold of ± 0.15 mW m^{-2} sr^{-1} nm^{-1} was then applied to the residual random error of the exponential model.

We used a hyperbolic model to relate GPP to SIF_d following Damm et al. (2015). This hyperbolic model approximates only the data behaviour and supports the theoretical argument that GPP saturates at moderate and high SIF_d level: $GPP = a \times \frac{SIF_d}{SIF_d + b}$; where a and b are fitted parameters. It is worth noting that a linear model between GPP and SIF_d was also investigated, and the results are provided in supplementary materials. Before relating GPP to SIF_d using this hyperbolic model at each site, SIF values equal or less than zero were discarded. Afterward, the same model was fitted on PFT scale by pooling all data across all sites for the same PFT. To explore the generalizability of the relationship between GPP and SIF_d, first the hyperbolic model was adjusted on data pooled across all sites. Second, to test further how the year, site and PFT, as categorical variables, and their interactions (year*GPP, site*GPP, and PFT*GPP) influence the GPP and SIF_d relationship, a Generalized Linear model (GLM) was used. Within the GLM model, SIF_d is considered as a response variable, whereas, site, PFT, year and GPP are the explanatory variables. These aforementioned variables and their interaction effects may affect the changes or variations either in SIF_d or GPP and consequently influence the slope and intercept of their relationships.

In order to study the synergy between SIF_d , R and VIs to improve GPP estimates, a Random Forest (RF) regression model was used (Brieman, 2001). Briefly, a RF is a machine learning algorithm, which combines the results of several randomly ensemble decision trees to reach a final accurate output. Before setting up the RF model, the correlation matrix between all variables was computed. It has been shown that features importance can be affected by the high correlation between feature predictors (Toloşi & Lengauer, 2011), suggesting that a decrease in importance values is observed when the level of correlation and the number of correlated variables increases. In practice, a strongly predictive variable belonging to a group of correlated variables can be considered less important than an independent and less informative variable. Based on remotely sensed data inputs and one categorical

explanatory variable (PFT), what variables are the most relevant for estimating GPP on daily data pooled altogether across all sites were evaluated. Four RF models were established relying on the combination of the predictive

210 variables to estimate GPP: (1) only surface spectral reflectance (RF-R), (2) surface spectral reflectance plus SIF_d (RF-SIF-R), (3) surface spectral reflectance plus SIF_d and the PFT as categorical variable (RF-SIF-R-PFT), and (4) SIF_d plus VIs (RF-SIF-VI) (namely NDVI, NIRv, and PRI). 80 per cent of the data were used for training and the remaining for testing the model. It is worth mentioning that a RandomizeSearchCV technique was used (Scikit-learn library for Python) to tune the model and took the best parameters for each model to predict GPP and applied

215 a 10-fold cross-validation and 20 iterations on the training set to avoid splitting the dataset into training, validating and testing sets which could affect the amount of data allocated for the training and could lead easily to model overfitting. The ensemble of decision tree models includes 200 trees for all models, but the number of splits per tree and the maximum depth varied. The relative importance of each variable, based on the mean decrease in impurity method, was used to evaluate the part of the contribution of each input variable in predicting the canopy

220 GPP variability. For TROPOMI data extraction, MATLAB R2021a (The MathWorks, Inc., USA) was used and python version 3.9.1 was used for data analysis and visualization (sklearn, scipy, seaborn, matplotlib, pandas, and numpy libraries for Python).

Ultimately, the strength of the relationships between SIF_d and GPP were compared based on the coefficient of determination (R^2), Root Mean Squared Error (RMSE), and the p-value metrics. The random forest models were

225 evaluated and compared based on out-of-bag adjusted R² and RMSE. At last, but not least, a paired t-test is used to compare the performance of the RF models based on the method proposed by (Nadeau et al., 2003). A 5% significance level was used for all statistical inference.

4.   Results

4.1   GPP vs SIF_d relationships

230 #### 4.1.1   Site-specific relationships

The first aim was to evaluate the strength of the relationships between tower-based GPP and SIF_d encompassing different vegetation types at site level. To do so, a hyperbolic model was used to relate GPP to SIF_d at each site. Figure 2 shows the relationships between GPP and SIF_d at each site. Overall, the results revealed a hyperbolic relationship with relatively saturating GPP in presence of moderate to high SIF_d. However, the relationships

235 between GPP and SIF_d are site-dependent, suggesting that the difference in plant functional types and spatial heterogeneity across sites may significantly affect the relationships between GPP and SIF_d. The strongest relationships were found at DK-Sor, FR-Fon, DE-Tha, SE-Nor and BE-Bra, which are DBF, ENF and MF vegetation type sites, with R^2 values being between 0.64 and 0.87 (p<0.0001). The weakest relationships were recorded at FI-Var, FR-EM2 and DE-RuW sites, and no significant relationship was found at GF-Guy, IT-Cp2 and

240 FR-Mej. For each fit, the numbers of data points were between 160 and 1510, depending on the data availability at each site. A detailed information and statistics on the relationships between GPP and SIF_d at each site is given in Supplementary Materials in Tab S3. Note that the independent assessment considering the linear model to relate SIF_d to GPP at each site, and each PFT and on data pooled across all sites revealed a relatively consistent lower goodness of fit, justifying the use of a hyperbolic model (see Supplementary Material Tab S4 and S5, Figures S1,

245 S2 and S3).
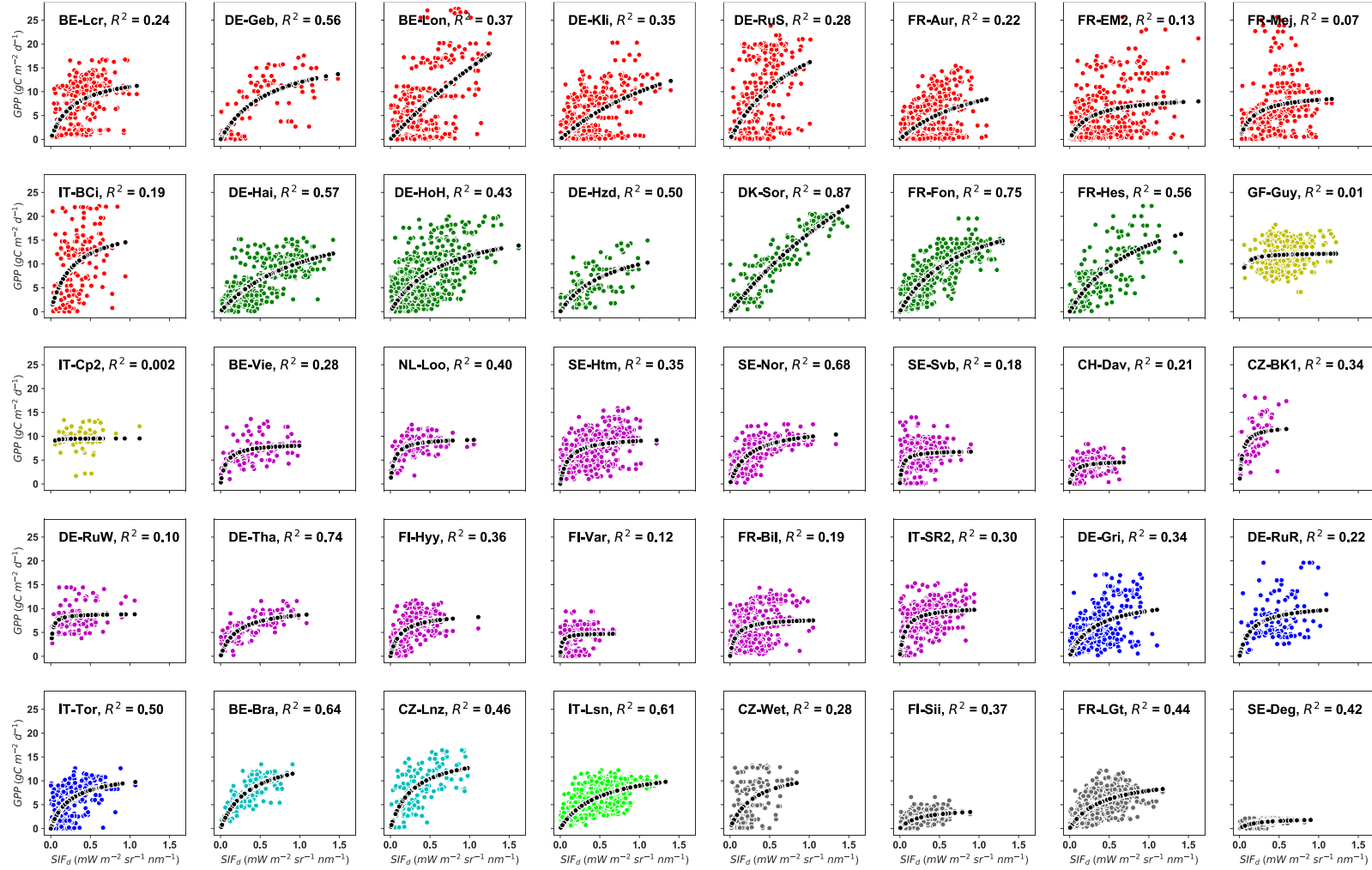
Figure 2: Site-specific tower-based GPP and SIF_d relationships at daily timescale. The R^2 represents the coefficient of determination of the relationship between GPP and SIF_d for each site. The color code represents the eight different plant functional types encountered in the study sites: Red color stands for CRO (croplands), green for DBF (deciduous broadleaf forests), yellow for EBF (evergreen broadleaf forests), magenta for ENF (evergreen needleleaf forests), blue for GRA (grasslands), Cyan for MF (mixed forests), lime for OSH (open shrubland), and dimgrey for WET (wetland). The black dotted line represents the hyperbolic fit between GPP and SIF_d.

250

4.1.2 Plant functional type-specific and overall sites relationships

To test the effects of the PFT on the relationship between GPP and SIF_d at the daily timescale, data were pooled across sites of the same PFT (MF, CRO, ENF, DBF, EBF, GRA, OSH, and WET) and the hyperbolic model was applied on each PFT. Figure 3 depicts the scatterplots of the relationships between GPP and SIF_d. The relationship between GPP and SIF_d was statistically significant for all PFT ($R^2 = 0.06$-0.61, p<0.0001), taken individually. Furthermore, the hyperbolic relationship between GPP and SIF_d was strongest for OSH, DBF and MF, with R^2 of 0.61, 0.59 and 0.52, respectively, and the lowest for EBF with R^2 of 0.06. This result suggests that the relationships between GPP and SIF_d were clearly PFT-specific, as shown in Table 2.
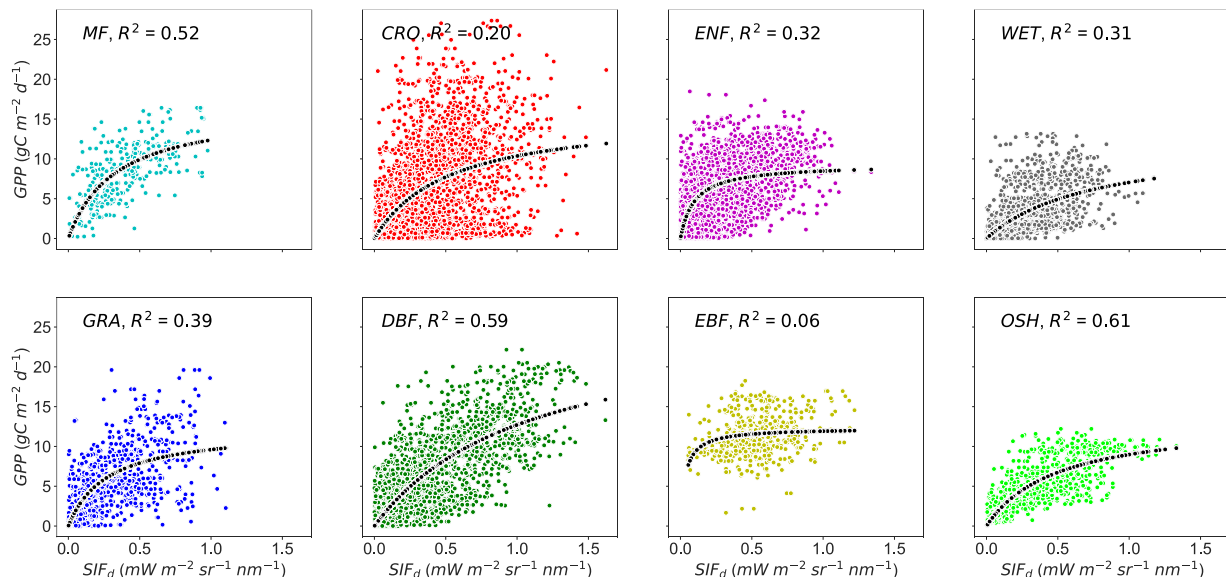
Figure 3: Relationships between tower-based GPP and SIF_d in eight plant functional types: MF, CRO, ENF, DBF, EBF, GRA, OSH, and WET at daily timescale. The R^2 represents the coefficient of determination of the relationship between GPP and SIF_d. All pairwise relationships between GPP vs SIF_d were statistically significant with p<0.0001. The black dotted line represents the hyperbolic fit between GPP and SIF_d.

Table 2: Summary statistics of plant functional type-specific GPP and SIF_d relationship in eight major PFT. All pairwise relationships between GPP and SIF_d were statistically significant with p<0.0001. a and b denote the fitted parameters from the hyperbolic model. The unit of RMSE is in (gC m^{-2} d^{-1}).

PFT	Sites	R^2	a	b	RMSE	N
CRO	9	0.20	15.74	0.52	5.29	5538
DBF	6	0.59	26.59	1.09	3.61	3566
EBF	2	0.06	12.31	0.03	2.66	956
ENF	13	0.32	9.30	0.10	2.94	6440
GRA	3	0.39	12.21	0.27	3.32	1658
MF	2	0.52	16.46	0.33	2.79	620
OSH	1	0.61	13.44	0.50	2.10	1510
WET	4	0.31	12.35	0.75	2.50	2710
ALL	40	0.36	15.33	0.45	3.93	22998

Moreover, the generalizability of the relationship between GPP and SIF_d was first tested on data pooled together across all sites (Figure 4). A significant but weak relationship between GPP and SIF_d was found across all sites with R^2 of 0.36 (p<0.0001) and RMSE of 3.93 gC m^{-2} d^{-1}. However, when the variations between the year, site and PFT as inputs variables were included in a GLM model, along with GPP, the results showed a strong significant

relationship between SIF$_d$, year, site, PFT and GPP (p<0.001). Furthermore, the interactions between year and

GPP, PFT and GPP were found to have statistically substantial effect on SIF$_d$ and GPP relationship, while the

275   interaction between site and GPP was not significant (see Supplementary Material in Tab S5). These findings

support that the GPP and SIF$_d$ relationship is considerably influenced by the site PFT and the interannual variations

in SIF$_d$.
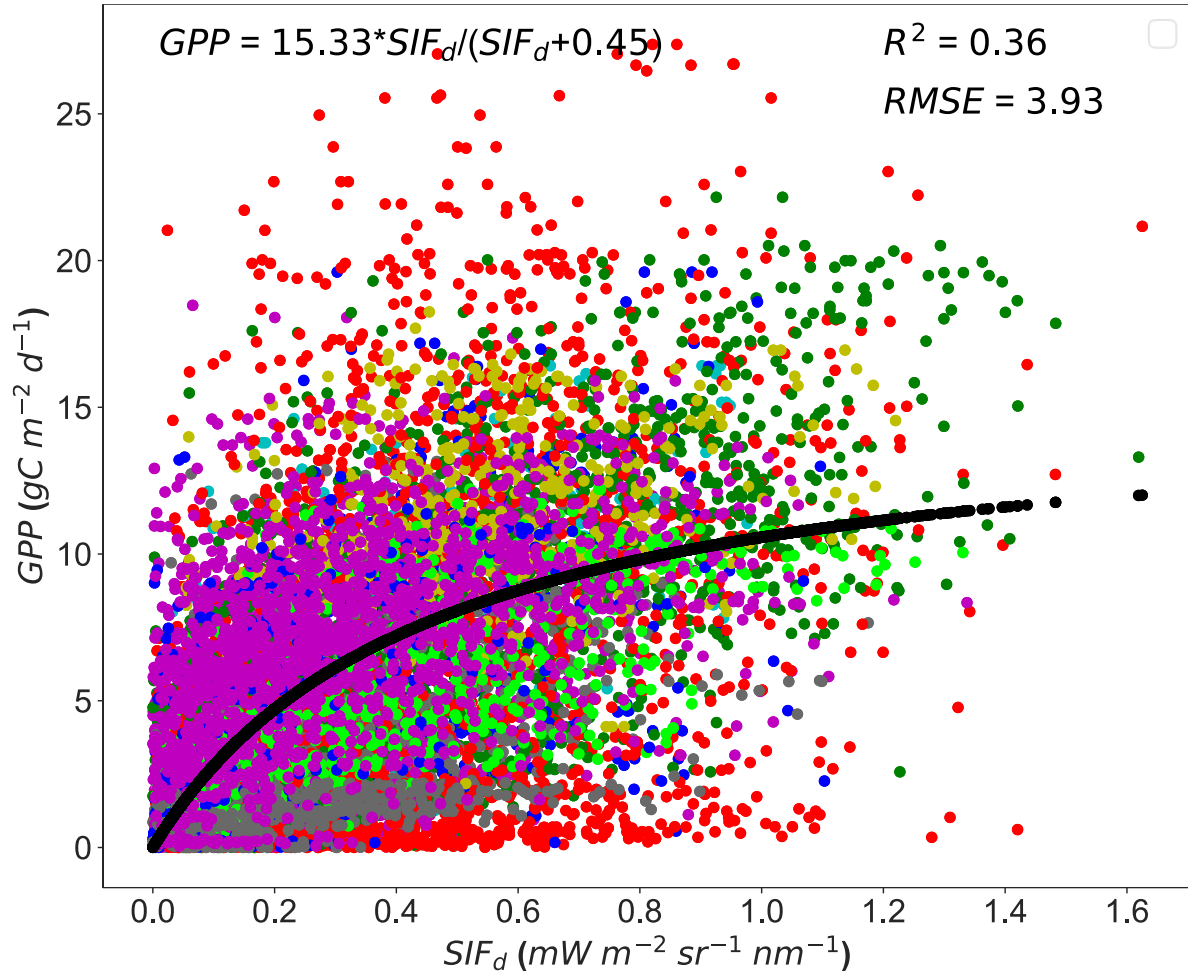
Figure 4: Scatterplots of the relationships between tower-based GPP and SIF$_d$ in eight PFT pooled together across all sites.
280   The black dotted line represents the hyperbolic fit between GPP and SIF$_d$. The color code represents the plant functional types
encountered in the study sites: Red color stands for CRO (croplands), green for DBF (deciduous broadleaf forests), yellow for
EBF (evergreen broadleaf forests), magenta for ENF (evergreen needleleaf forests), blue for GRA (grasslands), Cyan for MF
(mixed forests), lime for OSH (open shrubland), and dimgrey for WET (wetland).

4.2   Synergy between SIF$_d$, R and VIs to quantify GPP

285   In order to optimise the inputs for the Random Forest (RF) regression and avoid the effects of high correlated

explanatory variables on the model performance, the correlation matrix was computed. The correlation matrix

(supplied in Supplementary Materials Figure S4) revealed a strong dependency between predictive variables

(notably B$_9$ vs B$_{10}$, B$_{11}$ vs B$_{12}$ and B$_{13}$ vs B$_{14}$), indicating that using a RF model built in these variables could be

affected by those high correlations. Based on these observations, the R of B$_{10}$, B$_{12}$ and B$_{14}$ were excluded from the

290   explanatory variables of RF regression models.

4.2.1 Performance of GPP estimates using Random Forest regression

In Figure 5, it is represented tower-based GPP against the four RF GPP models across all sites. Overall, all the RF models predicted GPP show a high agreement with tower-based GPP. Yet, the RF-R model has the strongest relationship with tower-based GPP with an adjusted R^2 of 0.86 and RMSE of 1.72 gC m^{-2} d^{-1}, while the RF-SIF-VI model presents the lowest predictions of GPP as the adjusted R^2 and RMSE were 0.75 and 2.29 gC m^{-2} d^{-1}, respectively. Furthermore, the RF-SIF-R and RF-SIF-R-PFT model performed similarly well on estimating GPP as they could explain 82% and 83% of the variations in GPP across all sites, respectively. A paired t-test realized between the four models based on the adjusted R^2 performance revealed that the difference in adjusted R^2 between RF-R and RF-SIF-R, RF-R and RF-SIF-R-PFT, and RF-SIF-R and RF-SIF-R-PFT models was not statistically significant. In other words, these three RF models have statistically the same performance.
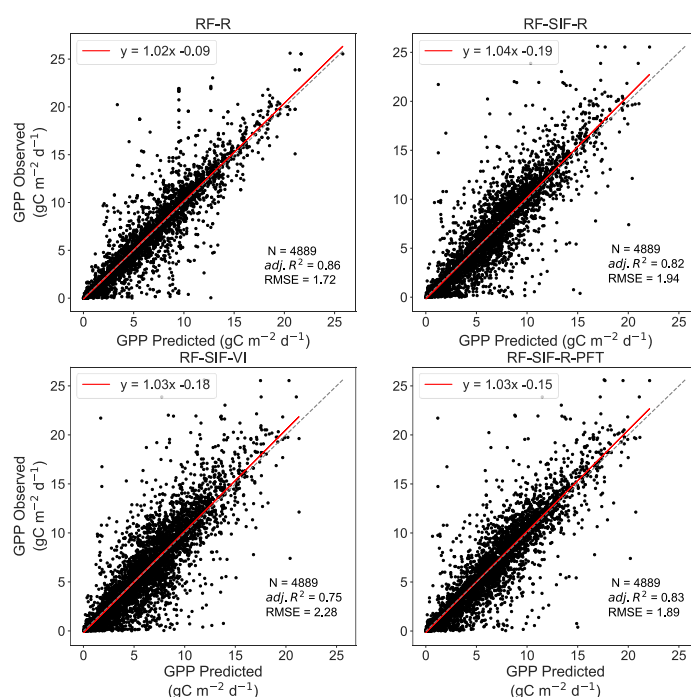
Figure 5: scatterplots of the observed GPP against the RF predicted GPP across all sites. The N denotes the number of data points used for the RF model's testing, adj. R^2 represents the adjusted coefficient of determination of the relationship between observed GPP and predicted GPP, and the RMSE is the Root Mean Squared Error between observed GPP and RF model predicted GPP. The dash diagonal line depicts the 1:1 line. RF-R denotes GPP prediction using only surface spectral reflectance, RF-SIF-R includes R and SIF$_d$ as inputs to predict GPP, RF-SIF-VI integrates SIF$_d$ and VIs to estimate GPP, and RF-SIF-R-PFT includes R, SIF$_d$ and plant functional type as categorical variable to predict GPP.

The RF regression model's GPP estimates and the observed GPP representing different vegetation types at the site level are depicted in the Figures 6 and 7 for the RF-SIF-R model predictions as an example. The estimates for each site from the others models are presented in the Supplementary Materials (Figures S6-a RF-R, S6-b RF-R, S7-a RF-SIF-VI, S7-b RF-SIF-VI, S8-a RF-SIF-R-PFT and S8-b RF-SIF-R-PFT) and the summary statistics results in Tab S7 for all RF models. At the site level, the RF-SIF-R model predicted tower-based GPP with high accuracy (adj. R^2 = 0.54-0.95), except for three sites such as *IT-BCi* (adj. R^2 = 0.21), *IT-Cp2* (adj. R^2 = 0.25), and *SE-Deg* (adj. R^2 = 0.41), where the RF-SIF-R model has difficulties to reproduce GPP, even if the R^2 remain statistically significant at 5% probability level. It is worth noting that all others RF

models have a poor GPP predictions for these aforementioned sites. However, on data pooled across all sites of the same PFT, the RF-SIF-R model show high performance in estimating GPP for all eight major PFT with an adj. R^2 being between 0.68 and 0.90. The lowest predictions are encountered in CRO and EBF sites, whereas the best tower-based GPP estimates were found in DBF and OSH sites.

320
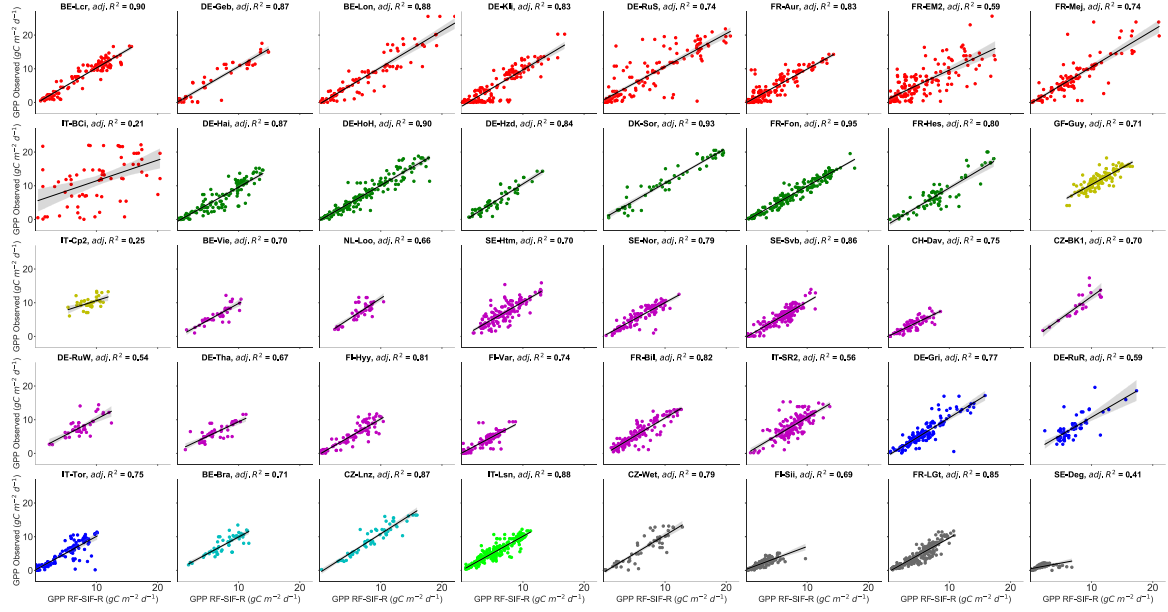
Figure 6: Site-specific scatterplots between observed GPP and RF-SIF-R predicted GPP at daily timescale. The adj. R^2 represents the adjusted coefficient of determination of the relationships between observed GPP and predicted GPP. All pairwise relationships between observed GPP vs predicted GPP were statistically significant at all sites (with p<0.0001). The color code 325 represents the eight different vegetation types encountered in the study sites: Red color stands for CRO, green for DBF, yellow for EBF, magenta for ENF, blue for GRA, Cyan for MF, lime for OSH, and dimgrey for WET.
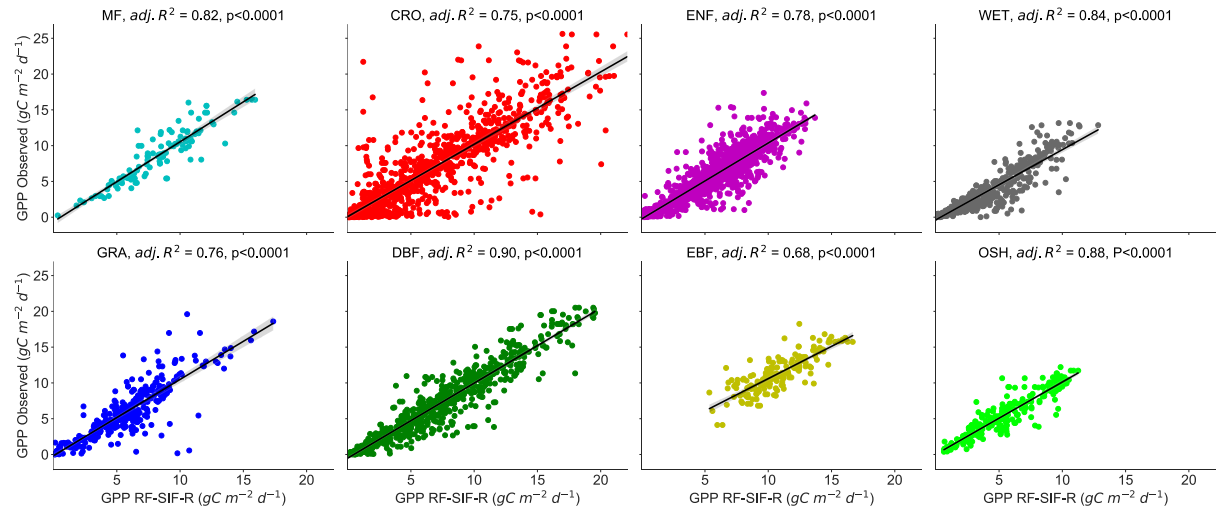
Figure 7: Scatterplots of observed GPP against RF-SIF-R predicted GPP in eight PFT at daily timescale. The adj. R^2 represents the adjusted coefficient of determination of the relationship between observed GPP and predicted GPP. p denotes probability 330 value of the relationships.

In Figure 8 and Table 3, it is depicted the observed and estimated GPP representing different PFT for all four RF models. The estimation for each site is given in Supplementary Materials Figure S5. Overall, all RF models' GPP predictions capture very well the seasonal and interannual dynamics of the tower-based GPP. However, there are sites, years and vegetation types where observed GPP cannot be estimated with high accuracy. For instance, the

335 RF models tend to underestimate GPP maxima in GRA, WET and EBF vegetation types. These underestimates are mostly marked by the slope of the relationships between the observed GPP and predicted GPP in Table 3.
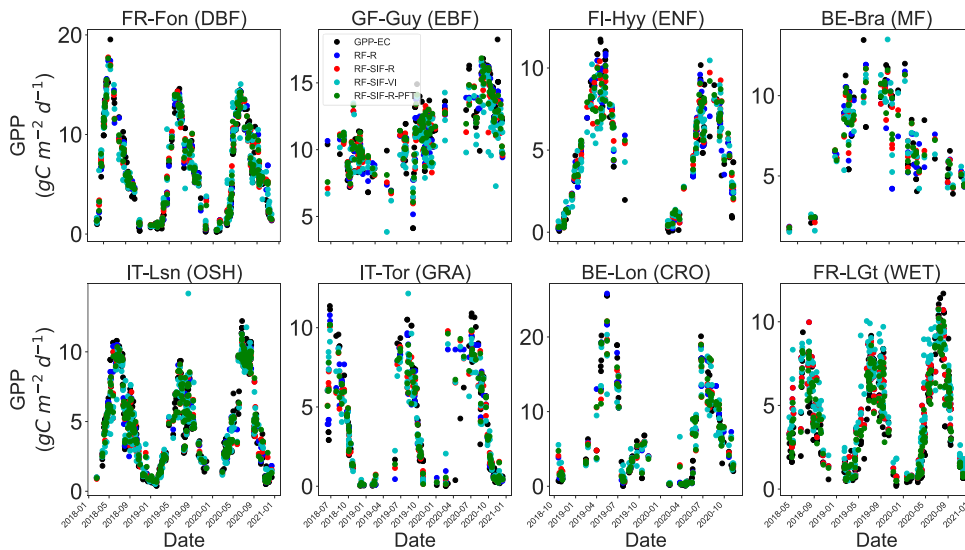
Figure 8: Comparison between observed GPP and RF regression models estimated GPP at selected ICOS flux sites representing different PFT: DBF, EBF, ENF, MF, CRO, GRA, OSH, and WET. The color code represents the different RF GPP predictions and the observed GPP: Red color stands for RF-SIF-R, green for RF-SIF-R-PFT, blue for RF-R, Cyan for RF-SIF-VI, and black for observed GPP.

Table 3: Summary statistics of plant functional type-specific observed GPP against RF models predicted GPP relationships in eight major PFT: MF, CRO, ENF, DBF, EBF, GRA, OSH, and WET. All pairwise relationships between observed GPP and predicted GPP were statistically significant with p<0.0001. The sign ± denotes the 95% confidence interval on the slope and intercept of the relationships between observed GPP and predicted GPP.

			RF-R				RF-SIF-R			
PFT	Sites	N	Adj. R^2	Slope	Intercept	RMSE	Adj. R^2	Slope	Intercept	RMSE
CRO	9	1171	0.78	1.03±0.03	0.00±0.24	2.67	0.75	1.01±0.03	0.08±0.26	2.89
DBF	6	748	0.92	1.02±0.02	-0.23±0.18	1.41	0.90	1.05±0.02	-0.52±0.21	1.61
EBF	2	188	0.77	0.93±0.07	1.01±0.83	1.23	0.68	0.90±0.09	1.58±0.99	1.45
ENF	13	1385	0.85	1.01±0.02	-0.01±15	1.29	0.78	1.06±0.03	-0.23±0.19	1.54
GRA	3	364	0.81	1.02±0.05	-0.02±32	1.64	0.76	1.07±0.06	-0.17±0.38	1.87
MF	2	117	0.84	1.05±0.08	-0.15±0.76	1.49	0.82	1.12±0.10	-0.62±0.83	1.56
OSH	1	317	0.91	1.02±0.04	-0.09±0.22	0.99	0.88	1.01±0.04	0.01±0.24	1.10
WET	4	599	0.92	0.98±0.02	-0.15±0.10	0.85	0.84	0.98±0.03	-0.37±0.15	1.17
ALL	40	4889	0.86	1.02±0.01	-0.09±0.08	1.72	0.82	1.04±0.01	-0.19±0.10	1.94
			RF-SIF-VI				RF-SIF-R-PFT			
PFT	Sites	N	Adj. R^2	Slope	Intercept	RMSE	Adj. R^2	Slope	Intercept	RMSE
CRO	9	1171	0.70	1.03±0.04	0.01±0.29	3.14	0.75	1.00±0.03	0.12±0.26	2.87
DBF	6	748	0.84	1.05±0.03	-0.58±0.28	2.06	0.91	1.04±0.02	-0.40±0.21	1.56
EBF	2	188	0.51	0.77±0.11	3.42±1.14	1.80	0.72	0.96±0.09	0.74±0.98	1.37
ENF	13	1385	0.66	1.02±0.04	0.10±0.24	1.92	0.79	1.08±0.03	-0.39±0.19	1.5
GRA	3	364	0.69	0.98±0.07	0.02±0.43	2.11	0.77	1.07±0.06	-0.29±0.38	1.84

MF	2	117	0.71	1.04±0.12	0.04±1.07	2.00	0.82	1.12±0.09	-0.73±0.84	1.56
OSH	1	317	0.83	0.98±0.05	0.21±0.29	1.33	0.89	1.02±0.04	-0.06±0.24	1.08
WET	4	599	0.72	0.88±0.04	-0.39±0.21	1.54	0.88	1.05±0.03	-0.29±0.12	0.99
ALL	40	4889	0.75	1.03±0.02	-0.18±0.12	2.28	0.83	1.03±0.01	-0.15±0.09	1.89

4.2.2 Relative importance of the predictive variables for predicting GPP

Figure 9 shows the relative importance (or mean decrease in impurity) of the predictive variables of the RF models for predicting GPP across all sites pooled together. The Figure 9 indicates that for RF-R model, the R in the near-infrared (NIR) band (B_2:841-876 nm) and the R in the red band (B_1: 620-670 nm) were found as the most important inputs variables for GPP estimates. Moreover, it can be seen that the contribution of the far-red R (B_{13}) on predicting GPP is also important, whereas the contribution of the others R bands was on similar level. For the RF-SIF-R model, SIF_d (>23%), R in the NIR (B_2 = 17%) and the R in the red band (B_1= 9%) are far largely the most relevant variables for GPP prediction, while the other variables contribute less into GPP estimates. The RF-SIF-R-PFT model differs with the previous model (RF-SIF-R) only on the plant functional type categorical variable and its results underline that the plant functional type variable is still important for predicting GPP. Ultimately, reflectance-based vegetation indices are widely used for predicting GPP at larger scales. Hence, it is worthwhile investigating what are the contributions of these interesting variables jointly with SIF_d in predicting canopy GPP. The relative importance derived from the RF-SIF-VI model reveals that SIF_d (36%) is substantially the most relevant variable for predicting GPP. The contributions of NIR_v and NDVI to the model are comparable, whereas PRI has a lower contribution in estimating GPP.
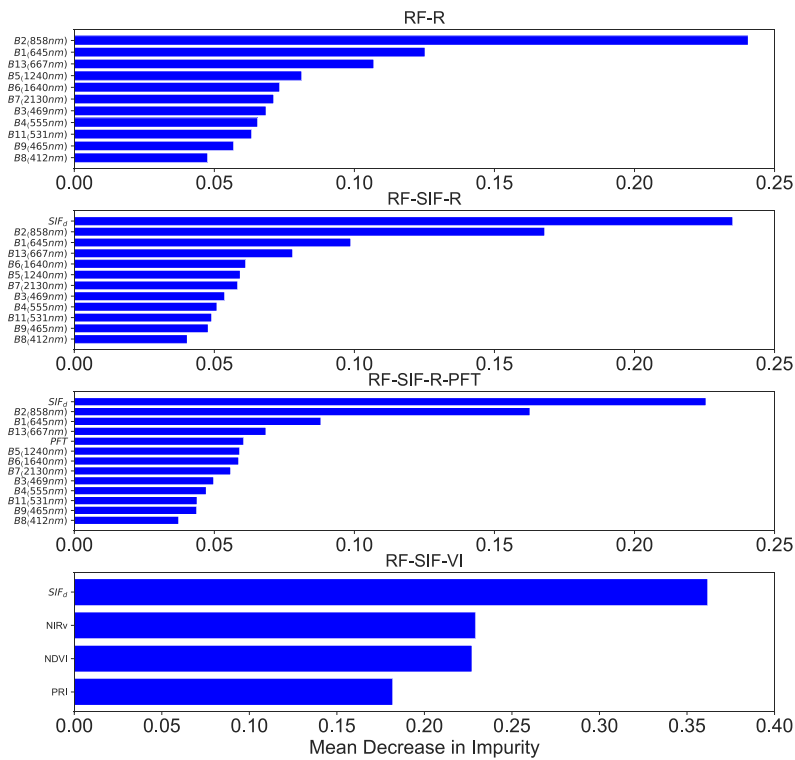
Figure 9: Relative importance of predictive variables of the RF models based only on remote sensing data for estimating GPP, except for the RF-SIF-R-PFT model. RF-R model based only on MODIS surface spectral reflectance, RF-SIF-R model uses

SIF$_d$ and surface reflectance as input variables, RF-SIF-R-PFT model integrates SIF$_d$, surface reflectance and PFT as explanatory variables, and RF-SIF-VI model combines SIF$_d$ and reflectance-based indices notably NDVI, NIR$_v$, and PRI as input variables for predicting GPP across all sites. The wavelengths depicted on the spectral bands denote the central wavelength

5.   Discussions

5.1   Strength of the relationship between GPP and SIF$_d$ at site and PFT levels

In this study, the first aim was to evaluate the strength of the relationship between tower-based GPP and SIF$_d$ at daily timescale and different spatial scales (at site and plant functional type levels).

At the site level, the results demonstrate that there were strong and statistically significant relationships between GPP and SIF$_d$. However, the hyperbolic fit between tower-based GPP and SIF$_d$ vary significantly across sites, which suggests a site-specific relationship. In other words, at these scales the differential variations in plant physiology and vegetation structure across sites and years and the spatiotemporal dynamics of the flux tower footprints (depending mainly on the height of the tower and wind direction), along with spatial heterogeneity and environmental conditions across sites may strongly affect first of all the SIF emissions, scattering and reabsorption across sites, and consequently the relationship between GPP and SIF$_d$ (Fournier et al., 2012; Paul-Limoges et al., 2018; Tagliabue et al., 2019; Li et al., 2020; Chu et al., 2021; Zhang, et al., 2021). These results are consistent with previous studies based on ground-based and satellite measurements which found evidence that canopy structure, as well as PFT have substantially great effects on the relationships between GPP and SIF across multiple sites (Dechant et al., 2020; Lu et al., 2020; Li et al., 2018; Sun et al., 2018; Wang et al., 2020; Hao et al., 2021; Wang et al., 2022). For instance, Wang et al. (2020) found that the relationship between OCO-2 SIF observed at 757 nm and 771 nm and tower-based GPP across eight vegetation types at 61 flux sites all over the world relies on canopy structure and Lu et al. (2020) reported a better relationship between canopy GPP and SIF corrected from reabsorption and scattering effects than top of canopy SIF based on ground-based measurements, underlying the importance of canopy structure on SIF and GPP relationships.

Furthermore, these results are also in good agreement with several studies carried out with instantaneous ground-based measurements at different vegetation types, sites and locations (Kim et al., 2021, Damm et al., 2015; He et al., 2020, Gu et al., 2019). For instance, Kim et al. (2021) pointed out that a hyperbolic model could explained better the relationships between GPP and SIF in an evergreen needle forest and Damm et al. (2015) showed similar results in croplands, mixed temperate forests and grassland vegetation types. One of the most plausible explanations is that GPP might reach saturation at high light, while SIF tends to keep increasing with PAR. It is also paramount to mention that the saturation of optical signal is a common issue in remote sensing, which can explain part of the lower relationships found in the EBF sites.

The relationship between tower-based GPP and SIF$_d$ considering the PFT was also examined. The results revealed a significant PFT-specific GPP and SIF$_d$ relationships across all eight major vegetation type. Yet, the hyperbolic relationships between GPP and SIF$_d$ vary considerably across PFT, suggesting a PFT-specific relationship. The relationship between GPP and SIF$_d$ is driven by the ratio of canopy photosynthesis and fluorescence yield, along with the canopy escape probability fraction of SIF photons from canopy to sensor (Porcar-Castell et al., 2014; Zhang et al., 2018; Zeng et al., 2019). The major drivers affecting the canopy photosynthesis and SIF yield include among others leaf morphology and orientation, plant physiology, canopy structure (leaf area index, chlorophyll contents, etc.), rapid changes in incident radiation and illuminated canopy surface, different contributions from photosystem I and II, as well as rapid abiotic responses (Porcar-Castell et al., 2014; Mohammed et al., 2019;

Gamon et al., 2019; P. Yang et al., 2020; Chu et al., 2021; Wang et al., 2022). These explanations altogether sustained the PFT-specific GPP vs SIF relationship as those factors can considerably differ across PFT. Additionally, the results showed that the MF, DBF and OSH sites have the strongest GPP and SIF_d relationship, which indicates that SIF may easily capture the seasonal, interannual and phenological variations in GPP within this vegetation type. In other words, in MF, DBF and OSH (one sample of vineyard plantation) biomes, there are explicitly marked seasonal and phenological changes compared to EBF or ENF forest where there is greenness all time. Thus, in DBF, MF and OSH biomes SIF signal may easily capture the variations in LAI and absorbed PAR and consequently display a high correlation between GPP and SIF_d. On the other hand, the lower observed relations between GPP and SIF_d in EBF (GF-Guy & IT-Cp2) sites could be partly explained by a lower spatiotemporal variability of SIF emissions in tropical forests coupled to a dispersed and lower GPP values observed on the datasets, as well as challenges in detecting or decoupling the understory vegetation effects from all vegetation canopy contribution to SIF emissions and uncertainties related to GPP estimates in tropical forests, while in CRO (FR-Mej) the difference in photosynthetic pathways (C3, C4 or mixed of both) and different management practices may be the reason why SIF_d could not capture the variations in GPP, as reported in early studies (Li et al., 2018; Hayek et al., 2018; Mengistu et al., 2020; He et al., 2020; Hornero et al., 2021; Li & Xiao, 2022). Previous studies have also reported weak relationships between GPP and SIF in EBF stands biome (Li et al., 2018; Wang et al., 2020). Moreover, it is worth mentioning that the biases related to cloudless sky and cloudy sky in space-based SIF retrieval, complicates the use of SIF to estimate GPP at the PFT scale because cloudless sky SIF and cloudless sky GPP are completely different from cloudy sky SIF and cloudy sky GPP and consequently, their relationship may also differ (Miao et al., 2018). Investigating GPP and SIF relationships based only on clear sky data and only on cloudy sky data, without the mix of both, is justified to better understand their links. Ultimately, not only the weak and statistically significant relationship reported for all biomes on data pooled together across all sites confirmed the PFT-dependent relationships between GPP and SIF_d in this study, but also the significant effects of the year, site and PFT in the relationship between SIF_d and GPP reported in the GLM model further supported this hypothesis. Exploring the newly launched satellite instruments such as OCO-3 and ECOSTRESS and upcoming FLEX and GeoCarb satellite missions which are planned to have diurnal sampling or fine-spatial resolution (for instance 300 m for FLEX), along with ongoing ground-based and airborne-based SIF and GPP data altogether will improve the abilities to not only better understand the GPP and SIF relationship but also to completely decouple the effects of driving factors such vegetation physiology, canopy structure and abiotic stress conditions that mediate their relationships at the ecosystem scale.

5.2   Synergy between SIF_d, R and VIs for estimating GPP using Random Forest

The second main goal in this manuscript was to explore the synergy between SIF_d from TROPOMI instrument and MODIS R and VIs namely NDVI, NIR_v and PRI for predicting GPP on data pooled across all sites. For achieving this purpose, four RF regression models were established: RF-R, RF-SIF-R, RF-SIF-R-PFT, and RF-SIF-VI. Except for RF-SIF-R-PFT model, the main advantage of using solely remotely sensed data for estimating GPP is that we do not need to rely on land cover type and land cover change, and meteorological data (Xiao et al., 2019). The current results show that the RF-R (surface spectral reflectance alone), RF-SIF-R (SIF_d plus surface spectral reflectance) and RF-SIF-R-PFT (SIF_d plus surface spectral reflectance plus PFT) models, statistically explain the same variance of GPP at the daily time scale (82~86%), whereas the RF-SIF-VI (SIF_d plus reflectance based-

indices) explains the lowest part, about 75% of GPP across all sites. It is well known that at the seasonal scale spectral reflectance capture the variations in canopy structure. The seasonal variations in canopy structure, especially LAI, are strongly correlated with variations in GPP (Dechant et al., 2022). This could justify the strong relationship found between tower-based GPP and the predicted GPP by the RF-R model. On the other hand, SIF is an integrative variable at the seasonal and interannual scales as shown in Figure 9 and on the correlation matrix results (strong contribution of SIF on GPP estimates and high correlation between GPP and SIF_d compared to each R band taken alone). However, SIF, while exhibiting the highest relative importance, fails to improve the GPP estimate. Hence, while being limited by its spatial resolution (7 km x 3.5 km), at which SIF may lose its physiological information and most likely reflect phenological, structural and illumination information (Jonard et al., 2020; Kimm et al., 2021), SIF remains a better predictor of GPP than each reflectance band individually. These results also revealed that the RF-SIF-VI have the poorest performance in predicting GPP. This lower performance could be partly due to the well-known saturation of VIs over dense canopies. In addition, the paired t-test did not show any statistically significant difference between RF-R and RF-SIF-R models, which confirms the above hypothesis, which suggests that SIF represents the variations in absorbed PAR at these scales. Recently, Pabon-Moreno et al. (2022) used solely Sentinel-2 satellite derived red-edge-based and near-infrared-based vegetation indices and all spectral bands to predict GPP at daily time scale across 54 EC flux sites using a data-driven approach (Random Forest). The authors reported that spectral bands jointly with VIs can inform only 66% of the variance in GPP, which is far less than the here worse performing model (i.e. RF-SIF-VI) in predicting GPP. The daily scale and solely remotely sensed driven RF-R and RF-SIF-R models outperform previous GPP products derived based on data-driven methods (Wolanin et al., 2019; Tramontana et al., 2016; Jung et al., 2019) and process-based model (Jiang & Ryu, 2016; Zhang et al., 2017; Lin et al., 2019), which included even further inputs as predictive variables such as meteorological data, land cover type and land cover change data and were conducted mostly at longer time scales (8-day or monthly time scale) compared to this study. Furthermore, these results are in strong agreement to two recent studies (Cho et al., 2021; Li et al., 2021). More specifically, Cho et al. (2021) found that remotely sensed data alone can explain 81% of GPP variability across four vegetation types, including ENF, EBF, DBF, and MF in South Korea at 8-day time scale and Li et al. (2021) pointed out that instantaneous GPP estimates across 56 flux tower sites could be achieved with a R^2 of 0.88 and RMSE of 2.42 µmol CO_2 m^{-2} s^{-1} using ECOSTRESS land surface temperature, daily MODIS satellite data and meteorological data from ERA5 reanalysis. This study revealed also that GPP prediction can be achieved with high accuracy based on solely remotely sensed data that are widely and publicly available for all.

The RF models could clearly capture the GPP variations at each site encompassing different vegetation types as shown in Figures 6 and 8. Indeed, there are sites, years and vegetation types where tower-based GPP were underestimated, which were the cases for WET and EBF vegetation types. Furthermore, all RF models suffer to estimate accurately tower GPP at *IT-BCi, IT-Cp2* and *SE-Deg* sites, owing most likely to SIF pixel heterogeneities and lower GPP values observed in these sites, along with previous explained issues associated in estimating GPP in crops and tropical stands. Similar results were reported recently in Pabon-Moreno et al. (2022) including eight vegetation types (ENF, CRO, DBF, GRA, WET, MF, SAV, and OSH). The reason behind these poor performances may be also related to difficulties to detect abiotic stress conditions (Bodesheim et al., 2018), underscoring the needs of more research for predicting GPP during extreme-abiotic conditions.

Furthermore, in this study, it is determined what are the main variables contributing to GPP prediction using the four RF models based on the relative importance metric of each model. Yet, it is found that SIF_d, the R in the NIR band (B_2), red band (B_1) and far-red band (B_{13}), as well as the vegetation type, NDVI and NIR_v seem to provide useful information for the predictions of GPP as shown in Figure 9. B_2 and B_1 are well-known spectral bands for characterizing vegetation canopy structure, seasonal phenology, canopy scattering and reabsorption due to chlorophyll content within leaves, and consequently have a dominant role in estimating GPP across all sites. The high contribution of SIF_d is presumably due to its integrative role at the seasonal and interannual scales as explained previously (Maguire et al., 2020; Dechant et al., 2022). PRI is known to be implied in the xanthophyll cycle, which is an important photoprotection mechanism and as a driver of GPP (Wang et al., 2020; Hmimina et al., 2015; Soudani et al., 2014). However, in this study, the findings evidenced that the contribution of PRI on predicting GPP was weak, which could be explained by the spatial and temporal aggregation of the rapid responses in plant physiological and functional activities, observable at the finer scales (diurnal). Ultimately, the findings in this study suggest that using R bands and SIF for estimating GPP is an important approach for improving GPP predictions compared to GPP products that include meteorological and land cover type information.

6.   Conclusion

In this current study, the strength of the relationships between tower-based GPP and SIF_d encompassing eight major plant functional types (PFT) at the site and interannual scales was evaluated, and the synergy between SIF_d, surface spectral reflectance, and reflectance-based indices namely NDVI, NIRv and PRI to improve GPP estimates using a data-driven modelling approach was examined.

At the site scale, the results showed a strong and statistically significant hyperbolic relationships between GPP and SIF_d ($p<0.0001$). However, these relationships were site-dependent, indicating that canopy structure and environmental conditions affect the relationship between GPP and SIF_d. The GPP and SIF_d relationships across all sites of the same PFT was considerably significant and was PFT-specific. Furthermore, it was also found that the relationships between GPP and SIF_d on data pooled across all sites was moderately weak but statistically significant, confirming the PFT dependence of the relationship between GPP and SIF_d. The GLM model results supported this PFT-dependent relationship between GPP and SIF_d as the site, year and PFT have meaningful effects on the slope of the relationship between GPP and SIF_d.

This study also demonstrated that the spectral reflectance bands, and SIF_d plus reflectance explained over 80% of the tower-based GPP variance. The RF models were able to represent the GPP seasonal and interannual variabilities across all sites. In addition, from the mean decrease in impurity results obtained from the RF models, it is inferred that the spectral reflectance bands in the near-infrared, red and SIF_d appeared as the most influential and dominant factors determining GPP predictions. In summary, this study provides insights into understanding the strength of the relationships between GPP and SIF across different ICOS flux sites and the use of the daily MODIS R and SIF_d TROPOMI on predicting GPP across different vegetation types.

Code and data availability. The computer codes (MATLAB and Python) used in this study are available upon demand from the corresponding author. Observations of carbon fluxes are available through the ICOS Data Portal services (https://www.icos-cp.eu/data-services p.eu). SIF data from TROPOMI instrument satellite are available through (https://data.caltech.edu/records/1347). Daily MODIS Aqua and Terra spectral reflectance data are

available through Google Earth Engine (https://earthengine.google.com/). Merged datasets are available on the request of the corresponding author.

Supplement. The supplementary materials related to this manuscript is available as a pdf document.

Author contributions. All authors contributed to the paper conceptualization. HB performed the data collection and preparation. HB and GH performed the data pre-processing, analyses and prepared the figures. HB led the writing of the manuscript with the contributions from all authors. KS, YG and GH supervised the project.

Competing interests. The authors declare that they have no conflict of interest.

Funding. This ongoing Ph.D work is jointly funded by le Centre National d'Études Spatiales (CNES) and ACRI-ST.

Acknowledgements. We thank Philip Köehler and Christian Frankenberg at Caltech for making TROPOMI SIF data available. We would also like to be thankful to all Integrated Carbon Observatory System (ICOS) PIs for providing the site level tower-based GPP data through the ICOS Data Portal services. Site names and locations are listed in Table 1 in Supplementary Material S1. We highly appreciate the supporting funding of CNES and le Programme National de Télédétection Spatiales (PNTS) across the ECOFLUO and C-FLEX projects, respectively. At last, not the least, we thank EIT Climate-KIC financial supports via the ARISE (Agriculture Resilience, Inclusive, and Sustainable Enterprise) project.

References

Badgley, G., Field, C. B., & Berry, J. A. (2017). Canopy near-infrared reflectance and terrestrial photosynthesis. *Science Advances*, *3*(3), Article 3. https://doi.org/10.1126/sciadv.1602244

Baldocchi, D. D., Ryu, Y., Dechant, B., Eichelmann, E., Hemes, K., Ma, S., Sanchez, C. R., Shortt, R., Szutu, D., Valach, A., Verfaillie, J., Badgley, G., Zeng, Y., & Berry, J. A. (2020). Outgoing Near-Infrared Radiation From Vegetation Scales With Canopy Photosynthesis Across a Spectrum of Function, Structure, Physiological Capacity, and Weather. *Journal of Geophysical Research: Biogeosciences*, *125*(7), Article 7. https://doi.org/10.1029/2019JG005534

Bodesheim, P., Jung, M., Gans, F., Mahecha, M. D., & Reichstein, M. (2018). *Upscaled diurnal cycles of land–atmosphere fluxes: A new global half-hourly data product*. 39.

Buchhorn, M., Smets, B., Bertels, L., Roo, B. D., Lesiv, M., Tsendbazar, N.-E., Li, L., & Tarko, A. (2020). *Copernicus Global Land Service: Land Cover 100m: version 3 Globe 2015-2019: Product User Manual* (Dataset v3.0, doc issue 3.3). Zenodo. https://doi.org/10.5281/ZENODO.3938963

555   Cho, S., Kang, M., Ichii, K., Kim, J., Lim, J.-H., Chun, J.-H., Park, C.-W., Kim, H. S., Choi, S.-W., Lee, S.-H., Indrawati, Y. M., & Kim, J. (2021). Evaluation of forest carbon uptake in South Korea using the national flux tower network, remote sensing, and data-driven technology. *Agricultural and Forest Meteorology*, *311*, 108653. https://doi.org/10.1016/j.agrformet.2021.108653

Chou, S., Chen, J., Yu, H., Chen, B., Zhang, X., Croft, H., Khalid, S., Li, M., & Shi, Q. (2017). Canopy-Level

560   Photochemical Reflectance Index from Hyperspectral Remote Sensing and Leaf-Level Non-Photochemical Quenching as Early Indicators of Water Stress in Maize. *Remote Sensing*, *9*(8), 794. https://doi.org/10.3390/rs9080794

Chu, H., Luo, X., Ouyang, Z., Chan, W. S., Dengel, S., Biraud, S. C., Torn, M. S., Metzger, S., Kumar, J., Arain, M. A., Arkebauer, T. J., Baldocchi, D., Bernacchi, C., Billesbach, D., Black, T. A., Blanken, P. D., Bohrer,

565   G., Bracho, R., Brown, S., … Zona, D. (2021). Representativeness of Eddy-Covariance flux footprints for areas surrounding AmeriFlux sites. *Agricultural and Forest Meteorology*, *301–302*, 108350. https://doi.org/10.1016/j.agrformet.2021.108350

Damm, A., Elbers, J., Erler, A., Gioli, B., Hamdi, K., Hutjes, R., Kosvancova, M., Meroni, M., Miglietta, F., Moersch, A., Moreno, J., Schickling, A., Sonnenschein, R., Udelhoven, T., Van Der LINDEN, S., Hostert,

570   P., & Rascher, U. (2010). Remote sensing of sun-induced fluorescence to improve modeling of diurnal courses of gross primary production (GPP): RS OF SUN-INDUCED FLUORESCENCE TO IMPROVE MODELING OF GPP. *Global Change Biology*, *16*(1), Article 1. https://doi.org/10.1111/j.1365-2486.2009.01908.x

Damm, A., Guanter, L., Paul-Limoges, E., van der Tol, C., Hueni, A., Buchmann, N., Eugster, W., Ammann, C.,

575   & Schaepman, M. E. (2015). Far-red sun-induced chlorophyll fluorescence shows ecosystem-specific relationships to gross primary production: An assessment based on observational and modeling approaches. *Remote Sensing of Environment*, *166*, 91–105. https://doi.org/10.1016/j.rse.2015.06.004

Daumard, F., Goulas, Y., Champagne, S., Fournier, A., Ounis, A., Olioso, A., & Moya, I. (2012). Continuous Monitoring of Canopy Level Sun-Induced Chlorophyll Fluorescence During the Growth of a Sorghum

580   Field. *IEEE Transactions on Geoscience and Remote Sensing*, *50*(11), Article 11. https://doi.org/10.1109/TGRS.2012.2193131

Dechant, B., Ryu, Y., Badgley, G., Köhler, P., Rascher, U., Migliavacca, M., Zhang, Y., Tagliabue, G., Guan, K., Rossini, M., Goulas, Y., Zeng, Y., Frankenberg, C., & Berry, J. A. (2022). NIRVP: A robust structural

proxy for sun-induced chlorophyll fluorescence and photosynthesis across scales. *Remote Sensing of*

585   *Environment*, *268*, 112763. https://doi.org/10.1016/j.rse.2021.112763

Dechant, B., Ryu, Y., Badgley, G., Zeng, Y., Berry, J. A., Zhang, Y., Goulas, Y., Li, Z., Zhang, Q., Kang, M., Li, J., & Moya, I. (2020). Canopy structure explains the relationship between photosynthesis and sun-induced chlorophyll fluorescence in crops. *Remote Sensing of Environment*, *241*, 111733. https://doi.org/10.1016/j.rse.2020.111733

590 Doughty, R., Xiao, X., Köhler, P., Frankenberg, C., Qin, Y., Wu, X., Ma, S., & Moore, B. (2021). Global-scale consistency of spaceborne vegetation indices, chlorophyll fluorescence, and photosynthesis. *Journal of Geophysical Research: Biogeosciences*. https://doi.org/10.1029/2020JG006136

Drolet, G. G., Middleton, E. M., Huemmrich, K. F., Hall, F. G., Amiro, B. D., Barr, A. G., Black, T. A., McCaughey, J. H., & Margolis, H. A. (2008). Regional mapping of gross light-use efficiency using

595   MODIS spectral indices. *Remote Sensing of Environment*, *112*(6), 3064–3078.

Drusch, M., Moreno, J., Del Bello, U., Franco, R., Goulas, Y., Huth, A., Kraft, S., Middleton, E. M., Miglietta, F., Mohammed, G., Nedbal, L., Rascher, U., Schuttemeyer, D., & Verhoef, W. (2017). The FLuorescence EXplorer Mission Concept—ESA's Earth Explorer 8. *IEEE Transactions on Geoscience and Remote Sensing*, *55*(3), 1273–1284. https://doi.org/10.1109/TGRS.2016.2621820

600 Falge, E., Baldocchi, D., Tenhunen, J., Aubinet, M., Bakwin, P., Berbigier, P., Bernhofer, C., Burba, G., Clement, R., Davis, K. J., Elbers, J. A., Goldstein, A. H., Grelle, A., Granier, A., Guðmundsson, J., Hollinger, D., Kowalski, A. S., Katul, G., Law, B. E., … Wofsy, S. (2002). Seasonality of ecosystem respiration and gross primary production as derived from FLUXNET measurements. *Agricultural and Forest Meteorology*, *113*(1–4), 53–74. https://doi.org/10.1016/S0168-1923(02)00102-8

605 Fournier, A., Daumard, F., Champagne, S., Ounis, A., Goulas, Y., & Moya, I. (2012). Effect of canopy structure on sun-induced chlorophyll fluorescence. *ISPRS Journal of Photogrammetry and Remote Sensing*, *68*, 112–120. https://doi.org/10.1016/j.isprsjprs.2012.01.003

Frankenberg, C., Fisher, J. B., Worden, J., Badgley, G., Saatchi, S. S., Lee, J.-E., Toon, G. C., Butz, A., Jung, M., Kuze, A., & Yokota, T. (2011). New global observations of the terrestrial carbon cycle from GOSAT:

610   Patterns of plant fluorescence with gross primary productivity: CHLOROPHYLL FLUORESCENCE FROM SPACE. *Geophysical Research Letters*, *38*(17), Article 17. https://doi.org/10.1029/2011GL048738

Gamon, J. A. (2015). Reviews and Syntheses: Optical sampling of the flux tower footprint. *Biogeosciences*, *12*(14), 4509–4523. https://doi.org/10.5194/bg-12-4509-2015

615 Gamon, J. A., Peñuelas, J., & Field, C. B. (1992). A narrow-waveband spectral index that tracks diurnal changes in photosynthetic efficiency. *Remote Sensing of Environment*, *41*(1), 35–44. https://doi.org/10.1016/0034-4257(92)90059-S

Gamon, J. A., Somers, B., Malenovský, Z., Middleton, E. M., Rascher, U., & Schaepman, M. E. (2019). Assessing Vegetation Function with Imaging Spectroscopy. *Surveys in Geophysics*, *40*(3), 489–513.
620 https://doi.org/10.1007/s10712-019-09511-5

Gitelson, A. A., Gamon, J. A., & Solovchenko, A. (2017). Multiple drivers of seasonal change in PRI: Implications for photosynthesis 2. Stand level. *Remote Sensing of Environment*, *190*, 198–206. https://doi.org/10.1016/j.rse.2016.12.015

Goulas, Y., Fournier, A., Daumard, F., Champagne, S., Ounis, A., Marloie, O., & Moya, I. (2017). Gross Primary
625 Production of a Wheat Canopy Relates Stronger to Far Red Than to Red Solar-Induced Chlorophyll Fluorescence. *Remote Sensing*, *9*(1), Article 1. https://doi.org/10.3390/rs9010097

Gu, L., Han, J., Wood, J. D., Chang, C. Y., & Sun, Y. (2019). Sun-induced Chl fluorescence and its importance for biophysical modeling of photosynthesis based on light reactions. *New Phytologist*, *223*(3), 1179–1191. https://doi.org/10.1111/nph.15796

630 Gu, L., Wood, J. D., Chang, C. Y. -Y., Sun, Y., & Riggs, J. S. (2019). Advancing Terrestrial Ecosystem Science With a Novel Automated Measurement System for Sun-Induced Chlorophyll Fluorescence for Integration With Eddy Covariance Flux Networks. *Journal of Geophysical Research: Biogeosciences*, *124*(1), Article 1. https://doi.org/10.1029/2018JG004742

Guanter, L., Bacour, C., Schneider, A., Aben, I., van Kempen, T. A., Maignan, F., Retscher, C., Köhler, P.,
635 Frankenberg, C., Joiner, J., & Zhang, Y. (2021). *The TROPOSIF global sun-induced fluorescence dataset from the Sentinel-5P TROPOMI mission* [Preprint]. Biosphere – Biogeosciences. https://doi.org/10.5194/essd-2021-199

Guanter, L., Frankenberg, C., Dudhia, A., Lewis, P. E., Gómez-Dans, J., Kuze, A., Suto, H., & Grainger, R. G. (2012). Retrieval and global assessment of terrestrial chlorophyll fluorescence from GOSAT space
640 measurements. *Remote Sensing of Environment*, *121*, 236–251. https://doi.org/10.1016/j.rse.2012.02.006

Guanter, L., Zhang, Y., Jung, M., Joiner, J., Voigt, M., Berry, J. A., Frankenberg, C., Huete, A. R., Zarco-Tejada, P., Lee, J.-E., Moran, M. S., Ponce-Campos, G., Beer, C., Camps-Valls, G., Buchmann, N., Gianelle, D.,

Klumpp, K., Cescatti, A., Baker, J. M., & Griffis, T. J. (2014). Global and time-resolved monitoring of crop photosynthesis with chlorophyll fluorescence. *Proceedings of the National Academy of Sciences*, *111*(14), Article 14. https://doi.org/10.1073/pnas.1320008111

Hao, D., Asrar, G. R., Zeng, Y., Yang, X., Li, X., Xiao, J., Guan, K., Wen, J., Xiao, Q., Berry, J. A., & Chen, M. (2021). Potential of hotspot solar-induced chlorophyll fluorescence for better tracking terrestrial photosynthesis. *Global Change Biology*, gcb.15554. https://doi.org/10.1111/gcb.15554

Hayek, M. N., Longo, M., Wu, J., Smith, M. N., Restrepo-Coupe, N., Tapajós, R., da Silva, R., Fitzjarrald, D. R., Camargo, P. B., Hutyra, L. R., Alves, L. F., Daube, B., Munger, J. W., Wiedemann, K. T., Saleska, S. R., & Wofsy, S. C. (2018). Carbon exchange in an Amazon forest: From hours to years. *Biogeosciences*, *15*(15), 4833–4848. https://doi.org/10.5194/bg-15-4833-2018

He, L., Magney, T., Dutta, D., Yin, Y., Köhler, P., Grossmann, K., Stutz, J., Dold, C., Hatfield, J., Guan, K., Peng, B., & Frankenberg, C. (2020). From the Ground to Space: Using Solar-Induced Chlorophyll Fluorescence to Estimate Crop Productivity. *Geophysical Research Letters*, *47*(7), Article 7. https://doi.org/10.1029/2020GL087474

Hilker, T., Coops, N. C., Nesic, Z., Wulder, M. A., & Black, A. T. (2007). Instrumentation and approach for unattended year round tower based measurements of spectral reflectance. *Computers and Electronics in Agriculture*, *56*(1), 72–84. https://doi.org/10.1016/j.compag.2007.01.003

Hilker, T., Lyapustin, A., Hall, F. G., Wang, Y., Coops, N. C., Drolet, G., & Black, T. A. (2009). An assessment of photosynthetic light use efficiency from space: Modeling the atmospheric and directional impacts on PRI reflectance. *Remote Sensing of Environment*, 13.

Hmimina, G., Merlier, E., Dufrêne, E., & Soudani, K. (2015). Deconvolution of pigment and physiologically related photochemical reflectance index variability at the canopy scale over an entire growing season: Towards an understanding of canopy PRI variability. *Plant, Cell & Environment*, *38*(8), 1578–1590. https://doi.org/10.1111/pce.12509

Hornero, A., North, P. R. J., Zarco-Tejada, P. J., Rascher, U., Martín, M. P., Migliavacca, M., & Hernandez-Clemente, R. (2021). Assessing the contribution of understory sun-induced chlorophyll fluorescence through 3-D radiative transfer modelling and field data. *Remote Sensing of Environment*, *253*, 112195. https://doi.org/10.1016/j.rse.2020.112195

Jiang, C., & Ryu, Y. (2016). Multi-scale evaluation of global gross primary productivity and evapotranspiration products derived from Breathing Earth System Simulator (BESS). *Remote Sensing of Environment*, *186*, 528–547. https://doi.org/10.1016/j.rse.2016.08.030

Jonard, F., De Cannière, S., Brüggemann, N., Gentine, P., Short Gianotti, D. J., Lobet, G., Miralles, D. G., Montzka, C., Pagán, B. R., Rascher, U., & Vereecken, H. (2020). Value of sun-induced chlorophyll fluorescence for quantifying hydrological states and fluxes: Current status and challenges. *Agricultural and Forest Meteorology*, *291*, 108088. https://doi.org/10.1016/j.agrformet.2020.108088

Jung, M., Koirala, S., Weber, U., Ichii, K., Gans, F., Camps-Valls, G., Papale, D., Schwalm, C., Tramontana, G., & Reichstein, M. (2019). The FLUXCOM ensemble of global land-atmosphere energy fluxes. *Scientific Data*, *6*(1), 74. https://doi.org/10.1038/s41597-019-0076-8

Kim, J., Ryu, Y., Dechant, B., Lee, H., Kim, H. S., Kornfeld, A., & Berry, J. A. (2021). Solar-induced chlorophyll fluorescence is non-linearly related to canopy photosynthesis in a temperate evergreen needleleaf forest during the fall transition. *Remote Sensing of Environment*, *258*, 112362. https://doi.org/10.1016/j.rse.2021.112362

Kimm, H., Guan, K., Jiang, C., Miao, G., Wu, G., Suyker, A. E., Ainsworth, E. A., Bernacchi, C. J., Montes, C. M., Berry, J. A., Yang, X., Frankenberg, C., Chen, M., & Köhler, P. (2021). A physiological signal derived from sun-induced chlorophyll fluorescence quantifies crop physiological response to environmental stresses in the U.S. Corn Belt. *Environmental Research Letters*, *16*(12), 124051. https://doi.org/10.1088/1748-9326/ac3b16

Köhler, P., Fischer, W. W., Rossman, G. R., Grotzinger, J. P., Doughty, R., Wang, Y., Yin, Y., & Frankenberg, C. (2021). Mineral Luminescence Observed From Space. *Geophysical Research Letters*, *48*(19). https://doi.org/10.1029/2021GL095227

Köhler, P., Frankenberg, C., Magney, T. S., Guanter, L., Joiner, J., & Landgraf, J. (2018). Global Retrievals of Solar-Induced Chlorophyll Fluorescence With TROPOMI: First Results and Intersensor Comparison to OCO-2. *Geophysical Research Letters*, *45*(19), Article 19. https://doi.org/10.1029/2018GL079031

Kong, J., Ryu, Y., Liu, J., Dechant, B., Rey-Sanchez, C., Shortt, R., Szutu, D., Verfaillie, J., Houborg, R., & Baldocchi, D. D. (2022). Matching high resolution satellite data and flux tower footprints improves their agreement in photosynthesis estimates. *Agricultural and Forest Meteorology*, *316*, 108878. https://doi.org/10.1016/j.agrformet.2022.108878

700   Li, J., Zhang, Y., Gu, L., Li, Z., Li, J., Zhang, Q., Zhang, Z., & Song, L. (2020). Seasonal variations in the relationship between sun-induced chlorophyll fluorescence and photosynthetic capacity from the leaf to canopy level in a rice crop. *Journal of Experimental Botany*, *71*(22), 7179–7197. https://doi.org/10.1093/jxb/eraa408

Li, X., & Xiao, J. (2022). TROPOMI observations allow for robust exploration of the relationship between solar-

705   induced chlorophyll fluorescence and terrestrial gross primary production. *Remote Sensing of Environment*, *268*, 112748. https://doi.org/10.1016/j.rse.2021.112748

Li, X., Xiao, J., Fisher, J. B., & Baldocchi, D. D. (2021). ECOSTRESS estimates gross primary production with fine spatial resolution for different times of day from the International Space Station. *Remote Sensing of Environment*, *258*, 112360. https://doi.org/10.1016/j.rse.2021.112360

710   Li, X., Xiao, J., & He, B. (2018). Chlorophyll fluorescence observed by OCO-2 is strongly related to gross primary productivity estimated from flux towers in temperate forests. *Remote Sensing of Environment*, *204*, 659–671. https://doi.org/10.1016/j.rse.2017.09.034

Li, X., Xiao, J., He, B., Altaf Arain, M., Beringer, J., Desai, A. R., Emmel, C., Hollinger, D. Y., Krasnova, A., Mammarella, I., Noe, S. M., Ortiz, P. S., Rey-Sanchez, A. C., Rocha, A. V., & Varlagin, A. (2018). Solar-

715   induced chlorophyll fluorescence is strongly correlated with terrestrial photosynthesis for a wide variety of biomes: First global analysis based on OCO-2 and flux tower observations. *Global Change Biology*, *24*(9), Article 9. https://doi.org/10.1111/gcb.14297

Lin, S., Li, J., Liu, Q., Li, L., Zhao, J., & Yu, W. (2019). Evaluating the Effectiveness of Using Vegetation Indices Based on Red-Edge Reflectance from Sentinel-2 to Estimate Gross Primary Productivity. *Remote*

720   *Sensing*, *11*(11), 1303. https://doi.org/10.3390/rs11111303

Lu, X., Liu, Z., Zhao, F., & Tang, J. (2020). Comparison of total emitted solar-induced chlorophyll fluorescence (SIF) and top-of-canopy (TOC) SIF in estimating photosynthesis. *Remote Sensing of Environment*, *251*, 112083. https://doi.org/10.1016/j.rse.2020.112083

Madani, N., Parazoo, N. C., Kimball, J. S., Ballantyne, A. P., Reichle, R. H., Maneta, M., Saatchi, S., Palmer, P.

725   I., Liu, Z., & Tagesson, T. (2020). Recent Amplified Global Gross Primary Productivity Due to Temperature Increase Is Offset by Reduced Productivity Due to Water Constraints. *AGU Advances*, *1*(4). https://doi.org/10.1029/2020AV000180

Magney, T. S., Bowling, D. R., Logan, B. A., Grossmann, K., Stutz, J., Blanken, P. D., Burns, S. P., Cheng, R., Garcia, M. A., Köhler, P., Lopez, S., Parazoo, N. C., Raczka, B., Schimel, D., & Frankenberg, C. (2019).

730   Mechanistic evidence for tracking the seasonality of photosynthesis with solar-induced fluorescence. *Proceedings of the National Academy of Sciences*, 201900278. https://doi.org/10.1073/pnas.1900278116

Maguire, A. J., Eitel, J. U. H., Griffin, K. L., Magney, T. S., Long, R. A., Vierling, L. A., Schmiege, S. C., Jennewein, J. S., Weygint, W. A., Boelman, N. T., & Bruner, S. G. (2020). On the Functional Relationship Between Fluorescence and Photochemical Yields in Complex Evergreen Needleleaf Canopies.
735   *Geophysical Research Letters*, *47*(9), Article 9. https://doi.org/10.1029/2020GL087858

Marrs, J. K., Reblin, J. S., Logan, B. A., Allen, D. W., Reinmann, A. B., Bombard, D. M., Tabachnik, D., & Hutyra, L. R. (2020). Solar-Induced Fluorescence Does Not Track Photosynthetic Carbon Assimilation Following Induced Stomatal Closure. *Geophysical Research Letters*, *47*(15). https://doi.org/10.1029/2020GL087956

740   Mengistu, A. G., Tsidu, G. M., Koren, G., Kooreman, M. L., Boersma, F., Tagesson, T., Ardö, J., Nouvellon, Y., & Peters, W. (2020). *Sun-induced Fluorescence and Near Infrared Reflectance of vegetation track the seasonal dynamics of gross primary production over Africa*. 23.

Meroni, M., Picchi, V., Rossini, M., Cogliati, S., Panigada, C., Nali, C., Lorenzini, G., & Colombo, R. (2008). Leaf level early assessment of ozone injuries by passive fluorescence and photochemical reflectance
745   index. *International Journal of Remote Sensing*, *29*(17–18), Article 17–18. https://doi.org/10.1080/01431160802036292

Miao, G., Guan, K., Yang, X., Bernacchi, C. J., Berry, J. A., DeLucia, E. H., Wu, J., Moore, C. E., Meacham, K., Cai, Y., Peng, B., Kimm, H., & Masters, M. D. (2018). Sun-Induced Chlorophyll Fluorescence, Photosynthesis, and Light Use Efficiency of a Soybean Field from Seasonally Continuous Measurements.
750   *Journal of Geophysical Research: Biogeosciences*, *123*(2), Article 2. https://doi.org/10.1002/2017JG004180

Mohammed, G. H., Colombo, R., Middleton, E. M., Rascher, U., van der Tol, C., Nedbal, L., Goulas, Y., Pérez-Priego, O., Damm, A., Meroni, M., Joiner, J., Cogliati, S., Verhoef, W., Malenovský, Z., Gastellu-Etchegorry, J.-P., Miller, J. R., Guanter, L., Moreno, J., Moya, I., … Zarco-Tejada, P. J. (2019). Remote
755   sensing of solar-induced chlorophyll fluorescence (SIF) in vegetation: 50 years of progress. *Remote Sensing of Environment*, *231*, 111177. https://doi.org/10.1016/j.rse.2019.04.030

Moureaux, C., Bodson, B., & Aubinet, M. (2008). Mesure des flux de CO2 et bilan carboné de grandes cultures: État de la question et méthodologie. *Biotechnol. Agron. Soc. Environ.*, 13.

Pabon-Moreno, D. E., Migliavacca, M., Reichstein, M., & Mahecha, M. D. (2022). On the potential of Sentinel-2 for estimating Gross Primary Production. *IEEE Transactions on Geoscience and Remote Sensing*, 1–1. https://doi.org/10.1109/TGRS.2022.3152272

Paul-Limoges, E., Damm, A., Hueni, A., Liebisch, F., Eugster, W., Schaepman, M. E., & Buchmann, N. (2018). Effect of environmental conditions on sun-induced fluorescence in a mixed forest and a cropland. *Remote Sensing of Environment*, *219*, 310–323. https://doi.org/10.1016/j.rse.2018.10.018

Porcar-Castell, A., Tyystjärvi, E., Atherton, J., van der Tol, C., Flexas, J., Pfündel, E. E., Moreno, J., Frankenberg, C., & Berry, J. A. (2014). Linking chlorophyll a fluorescence to photosynthesis for remote sensing applications: Mechanisms and challenges. *Journal of Experimental Botany*, *65*(15), Article 15. https://doi.org/10.1093/jxb/eru191

Randomforest2001.pdf. (n.d.).

Running, S. W., Nemani, R. R., Heinsch, F. A., Zhao, M., Reeves, M., & Hashimoto, H. (2004). A Continuous Satellite-Derived Measure of Global Terrestrial Primary Production. *BioScience*, *54*(6), 547. https://doi.org/10.1641/0006-3568(2004)054[0547:ACSMOG]2.0.CO;2

Sippel, S., Reichstein, M., Ma, X., Mahecha, M. D., Lange, H., Flach, M., & Frank, D. (2018). Drought, Heat, and the Carbon Cycle: A Review. *Current Climate Change Reports*, *4*(3), 266–286. https://doi.org/10.1007/s40641-018-0103-4

Smith, W. K., Biederman, J. A., Scott, R. L., Moore, D. J. P., He, M., Kimball, J. S., Yan, D., Hudson, A., Barnes, M. L., MacBean, N., Fox, A. M., & Litvak, M. E. (2018). Chlorophyll Fluorescence Better Captures Seasonal and Interannual Gross Primary Productivity Dynamics Across Dryland Ecosystems of Southwestern North America. *Geophysical Research Letters*, *45*(2), Article 2. https://doi.org/10.1002/2017GL075922

Soudani, K., Hmimina, G., Dufrêne, E., Berveiller, D., Delpierre, N., Ourcival, J.-M., Rambal, S., & Joffre, R. (2014). Relationships between photochemical reflectance index and light-use efficiency in deciduous and evergreen broadleaf forests. *Remote Sensing of Environment*, *144*, 73–84. https://doi.org/10.1016/j.rse.2014.01.017

Sun, Y., Frankenberg, C., Jung, M., Joiner, J., Guanter, L., Köhler, P., & Magney, T. (2018). Overview of Solar-Induced chlorophyll Fluorescence (SIF) from the Orbiting Carbon Observatory-2: Retrieval, cross-mission comparison, and global monitoring for GPP. *Remote Sensing of Environment*, *209*, 808–823. https://doi.org/10.1016/j.rse.2018.02.016

Tagliabue, G., Panigada, C., Dechant, B., Baret, F., Cogliati, S., Colombo, R., Migliavacca, M., Rademske, P., Schickling, A., Schüttemeyer, D., Verrelst, J., Rascher, U., Ryu, Y., & Rossini, M. (2019). Exploring the spatial relationship between airborne-derived red and far-red sun-induced fluorescence and process-based GPP estimates in a forest ecosystem. *Remote Sensing of Environment*, *231*, 111272. https://doi.org/10.1016/j.rse.2019.111272

Toloşi, L., & Lengauer, T. (2011). Classification with correlated features: Unreliability of feature ranking and solutions. *Bioinformatics*, *27*(14), 1986–1994. https://doi.org/10.1093/bioinformatics/btr300

Tramontana, G., Jung, M., Schwalm, C. R., Ichii, K., Camps-Valls, G., Ráduly, B., Reichstein, M., Arain, M. A., Cescatti, A., Kiely, G., Merbold, L., Serrano-Ortiz, P., Sickert, S., Wolf, S., & Papale, D. (2016). Predicting carbon dioxide and energy fluxes across global FLUXNET sites withregression algorithms. *Biogeosciences*, *13*(14), 4291–4313. https://doi.org/10.5194/bg-13-4291-2016

Tucker, C. J. (1979). Red and photographic infrared linear combinations for monitoring vegetation. *Remote Sensing of Environment*, *8*(2), 127–150.

Vermote, P. E. F., Roger, J. C., & Ray, J. P. (2015). *MODIS Land Surface Reflectance Science Computing Facility Principal Investigator: Dr. Eric F. Vermote Web site: Http://modis-sr.ltdri.org Correspondence e-mail address: Mod09@ltdri.org*. 35.

Wang, N., Suomalainen, J., Bartholomeus, H., Kooistra, L., Masiliūnas, D., & Clevers, J. G. P. W. (2021). Diurnal variation of sun-induced chlorophyll fluorescence of agricultural crops observed from a point-based spectrometer on a UAV. *International Journal of Applied Earth Observation and Geoinformation*, *96*, 102276. https://doi.org/10.1016/j.jag.2020.102276

Wang, X., Biederman, J. A., Knowles, J. F., Scott, R. L., Turner, A. J., Dannenberg, M. P., Köhler, P., Frankenberg, C., Litvak, M. E., Flerchinger, G. N., Law, B. E., Kwon, H., Reed, S. C., Parton, W. J., Barron-Gafford, G. A., & Smith, W. K. (2022). Satellite solar-induced chlorophyll fluorescence and near-infrared reflectance capture complementary aspects of dryland vegetation productivity dynamics. *Remote Sensing of Environment*, *270*, 112858. https://doi.org/10.1016/j.rse.2021.112858

Wang, X., Chen, J. M., & Ju, W. (2020). Photochemical reflectance index (PRI) can be used to improve the relationship between gross primary productivity (GPP) and sun-induced chlorophyll fluorescence (SIF). *Remote Sensing of Environment*, *246*, 111888. https://doi.org/10.1016/j.rse.2020.111888

Wieneke, S., Ahrends, H., Damm, A., Pinto, F., Stadler, A., Rossini, M., & Rascher, U. (2016). Airborne based spectroscopy of red and far-red sun-induced chlorophyll fluorescence: Implications for improved

estimates of gross primary productivity. *Remote Sensing of Environment*, *184*, 654–667. https://doi.org/10.1016/j.rse.2016.07.025

Wieneke, S., Burkart, A., Cendrero-Mateo, M. P., Julitta, T., Rossini, M., Schickling, A., Schmidt, M., & Rascher, U. (2018). Linking photosynthesis and sun-induced fluorescence at sub-daily to seasonal scales. *Remote Sensing of Environment*, *219*, 247–258. https://doi.org/10.1016/j.rse.2018.10.019

Wolanin, A., Camps-Valls, G., Gómez-Chova, L., Mateo-García, G., van der Tol, C., Zhang, Y., & Guanter, L. (2019). Estimating crop primary productivity with Sentinel-2 and Landsat 8 using machine learning methods trained with radiative transfer simulations. *Remote Sensing of Environment*, *225*, 441–457. https://doi.org/10.1016/j.rse.2019.03.002

Wood, J. D., Griffis, T. J., Baker, J. M., Frankenberg, C., Verma, M., & Yuen, K. (2017). Multiscale analyses of solar-induced florescence and gross primary production: Multiscale GPP-SIF RELATIONS. *Geophysical Research Letters*, *44*(1), 533–541. https://doi.org/10.1002/2016GL070775

Wu, G., Guan, K., Jiang, C., Peng, B., Kimm, H., Chen, M., Yang, X., Wang, S., Suyker, A. E., Bernacchi, C. J., Moore, C. E., Zeng, Y., Berry, J. A., & Cendrero-Mateo, M. P. (2020). Radiance-based NIR $_v$ as a proxy for GPP of corn and soybean. *Environmental Research Letters*, *15*(3), 034009. https://doi.org/10.1088/1748-9326/ab65cc

Xiao, J., Chevallier, F., Gomez, C., Guanter, L., Hicke, J. A., Huete, A. R., Ichii, K., Ni, W., Pang, Y., Rahman, A. F., Sun, G., Yuan, W., Zhang, L., & Zhang, X. (2019). Remote sensing of the terrestrial carbon cycle: A review of advances over 50 years. *Remote Sensing of Environment*, *233*, 111383. https://doi.org/10.1016/j.rse.2019.111383

Xiao, X. (2004). Modeling gross primary production of temperate deciduous broadleaf forest using satellite images and climate data. *Remote Sensing of Environment*, *91*(2), 256–270. https://doi.org/10.1016/j.rse.2004.03.010

Yang, H., Yang, X., Zhang, Y., Heskel, M. A., Lu, X., Munger, J. W., Sun, S., & Tang, J. (2017). Chlorophyll fluorescence tracks seasonal variations of photosynthesis from leaf to canopy in a temperate forest. *Global Change Biology*, *23*(7), Article 7. https://doi.org/10.1111/gcb.13590

Yang, P., Van der Tol, C., Campbell, P. K. E., & Middleton, E. M. (2020). *Unravelling the physical and physiological basis for the solar-inducedchlorophyll fluorescence and photosynthesis relationship* [Preprint]. Biodiversity and Ecosystem Function: Terrestrial. https://doi.org/10.5194/bg-2020-323

Yang, X., Tang, J., Mustard, J. F., Lee, J.-E., Rossini, M., Joiner, J., Munger, J. W., Kornfeld, A., & Richardson, A. D. (2015). Solar-induced chlorophyll fluorescence that correlates with canopy photosynthesis on diurnal and seasonal scales in a temperate deciduous forest: Fluorescence and photosynthesis. *Geophysical Research Letters*, *42*(8), Article 8. https://doi.org/10.1002/2015GL063201

Yazbeck, T., Bohrer, G., Gentine, P., Ye, L., Arriga, N., Bernhofer, C., Blanken, P. D., Desai, A. R., Durden, D., Knohl, A., Kowalska, N., Metzger, S., Mölder, M., Noormets, A., Novick, K., Scott, R. L., Šigut, L., Soudani, K., Ueyama, M., & Varlagin, A. (2021). Site Characteristics Mediate the Relationship Between Forest Productivity and Satellite Measured Solar Induced Fluorescence. *Frontiers in Forests and Global Change*, *4*, 695269. https://doi.org/10.3389/ffgc.2021.695269

Zeng, Y., Badgley, G., Dechant, B., Ryu, Y., Chen, M., & Berry, J. A. (2019). A practical approach for estimating the escape ratio of near-infrared solar-induced chlorophyll fluorescence. *Remote Sensing of Environment*, *232*, 111209. https://doi.org/10.1016/j.rse.2019.05.028

Zhang, J., Xiao, J., Tong, X., Zhang, J., Meng, P., Li, J., Liu, P., & Yu, P. (2022). NIRv and SIF better estimate phenology than NDVI and EVI: Effects of spring and autumn phenology on ecosystem production of planted forests. *Agricultural and Forest Meteorology*, *315*, 108819. https://doi.org/10.1016/j.agrformet.2022.108819

Zhang, Y., Migliavacca, M., Penuelas, J., & Ju, W. (2021). Advances in hyperspectral remote sensing of vegetation traits and functions. *Remote Sensing of Environment*, *252*, 112121. https://doi.org/10.1016/j.rse.2020.112121

Zhang, Y., Xiao, X., Wu, X., Zhou, S., Zhang, G., Qin, Y., & Dong, J. (2017). A global moderate resolution dataset of gross primary production of vegetation for 2000–2016. *Scientific Data*, *4*(1), 170165. https://doi.org/10.1038/sdata.2017.165

Zhang, Y., Xiao, X., Zhang, Y., Wolf, S., Zhou, S., Joiner, J., Guanter, L., Verma, M., Sun, Y., Yang, X., Paul-Limoges, E., Gough, C. M., Wohlfahrt, G., Gioli, B., van der Tol, C., Yann, N., Lund, M., & de Grandcourt, A. (2018). On the relationship between sub-daily instantaneous and daily total gross primary production: Implications for interpreting satellite-based SIF retrievals. *Remote Sensing of Environment*, *205*, 276–289. https://doi.org/10.1016/j.rse.2017.12.009

Zhang, Y., Zhang, Q., Liu, L., Zhang, Y., Wang, S., Ju, W., Zhou, G., Zhou, L., Tang, J., Zhu, X., Wang, F., Huang, Y., Zhang, Z., Qiu, B., Zhang, X., Wang, S., Huang, C., Tang, X., & Zhang, J. (2021). ChinaSpec:

A Network for Long-term Ground-based Measurements of Solar-induced Fluorescence in China. *Journal of Geophysical Research: Biogeosciences*. https://doi.org/10.1029/2020JG006042

Zhang, Z., Zhang, Y., Porcar-Castell, A., Joiner, J., Guanter, L., Yang, X., Migliavacca, M., Ju, W., Sun, Z., Chen, S., Martini, D., Zhang, Q., Li, Z., Cleverly, J., Wang, H., & Goulas, Y. (2020). Reduction of structural impacts and distinction of photosynthetic pathways in a global estimation of GPP from space-borne solar-induced chlorophyll fluorescence. *Remote Sensing of Environment*, *240*, 111722. https://doi.org/10.1016/j.rse.2020.111722

Supplementary materials of

Synergy between TROPOMI sun-induced chlorophyll fluorescence and MODIS spectral reflectance for understanding the dynamics of gross primary productivity at integrated carbon observatory system (ICOS) ecosystem flux sites

Hamadou Balde[1,2], Gabriel Hmimina[1], Yves Goulas[1], Gwendal Latouche[2], Kamel Soudani[2]

Correspondence to: Hamadou Balde (hamadou.balde@lmd.ispl.fr)

Tab S1: Information on the sites used in this study from the ICOS release 2018 and 2021. The PFT represents the plant functional type corresponding to each site: MF (mixed forests), CRO (croplands), DBF (deciduous broadleaf forests), EBF (evergreen broadleaf forests), ENF (evergreen needleleaf forests), GRA (grasslands), OSH (open shrublands), and WET (wetlands). Years denote the year of data flux available for each site.

Site name	Latitude (°)	Longitude (°)	PFT	Years
BE-Bra	51.307617	4.519844	MF	2018
BE-Lcr	51.112184	3.850433	CRO	2019, 2020
BE-Lon	50.551586	4.7461305	CRO	2019, 2020
BE-Vie	50.305068	5.998052	ENF	2018
CH-Dav	46.815283	9.855009	ENF	2018, 2019, 2020
CZ-BK1	49.50213	18.53685	ENF	2018
CZ-Lnz	48.681611	16.946416	MF	2018
CZ-Wet	49.024657	14.7703419	WET	2018
DE-Geb	51.099714	10.914629	CRO	2018
DE-Gri	50.950046	13.512681	GRA	2018, 2019, 2020
DE-Hai	51.079189	10.452336	DBF	2018, 2019, 2020
DE_HoH	52.086484	11.222468	DBF	2018, 2019, 2020
DE-Hzd	50.963566	13.490172	DBF	2018
DE-Kli	50.892881	13.5225056	CRO	2018, 2019, 2020
DE-RuR	50.621914	6.3041256	GRA	2018
DE-RuS	50.865912	6.4471689	CRO	2018, 2019, 2020
DE-RuW	50.504907	6.33101886	ENF	2018
DE-Tha	50.962631	13.565225	ENF	2018

DK-Sor	55.485869	11.644644	DBF	2018
FI-Hyy	61.84741	24.29477	ENF	2018, 2020
FI-Sii	61.832683	24.19278333	WET	2018, 2019, 2020
FI-Var	67.7549	29.61	ENF	2018, 2019, 2020
FR-Aur	43.54965	1.10615	CRO	2019, 2020
FR-Bil	44.49389	-0.95592	ENF	2018, 2019, 2020
FR-EM2	49.872108	3.02065	CRO	2018, 2019, 2020
FR-Fon	48.476339	2.780136	DBF	2018, 2019, 2020
FR-Hes	48.84415	1.951910019	DBF	2018
FR-LGt	48.67416	7.06461667	WET	2018, 2019, 2020
FR-Mej	48.117707	-1.798283	CRO	2019, 2020
GF-Guy	5.2787	-52.9248	EBF	2018, 2019, 2020
IT-BCi	40.52375	14.957444	CRO	2018
IT-Cp2	41.704267	12.357293	EBF	2018
IT-Lsn	45.740481	12.750297	OSH	2018, 2019, 2020
IT-SR2	43.73203	10.29095	ENF	2018, 2019, 2020
IT-Tor	45.844444	7.578055556	GRA	2018, 2019, 2020
NL-Loo	52.16648	5.74355	ENF	2018
SE-Deg	64.182	19.556694	WET	2018, 2020
SE-Htm	56.09763	13.41897	ENF	2018, 2019, 2020
SE-Nor	60.086441	17.479455	ENF	2018, 2019, 2020
SE-Svb	64.256097	19.77451111	ENF	2018, 2019, 2020

Tab S2: MODIS Terra and Aqua surface spectral reflectance bands. NIR denotes for near-infrared, SWNIR for shortwave near-infrared, SWIR shortwave infrared, and VNIR visible near-infrared.

Acronym	Full Name	Wavelengths (nm)	**Band name**	Spatial Resolution
B_1	Surface Reflectance for B_1	620-670	**Red**	500 m
B_2	Surface Reflectance for B_2	841-876	**NIR**	
B_3	Surface Reflectance for B_3	459-479	**Blue**	
B_4	Surface Reflectance for B_4	545-565	**Green**	

B$_5$	Surface Reflectance for B$_5$	1230-1250	**SWNIR**	
B$_6$	Surface Reflectance for B$_6$	1628-1652	**SWIR**	
B$_7$	Surface Reflectance for B$_7$	2105-2155	**SWIR**	
B$_8$	Surface Reflectance for B$_8$	405-420	**Blue**	1 km
B$_9$	Surface Reflectance for B$_9$	438-448	**Blue**	
B$_{10}$	Surface Reflectance for B$_{10}$	483-493	**Blue**	
B$_{11}$	Surface Reflectance for B$_{11}$	526-536	**Green**	
B$_{12}$	Surface Reflectance for B$_{12}$	546-556	**Green**	
B$_{13}$	Surface Reflectance for B$_{13}$	662-672	**Red**	
B$_{14}$	Surface Reflectance for B$_{14}$	673-683	**VNIR**	
B$_{15}$	Surface Reflectance for B$_{15}$	743-753	**VNIR**	
B$_{16}$	Surface Reflectance for B$_{16}$	862-877	**NIR**	

Tab S3: Detailed results and statistics of the site-specific hyperbolic relationships between GPP and SIF$_d$. R^2 denotes for the coefficient of determination. The unit of RMSE (Root Mean Squared Error) is in (gC m^{-2} d^{-1}). PFT represents the plant functional type of each site: MF (mixed forests), CRO (croplands), DBF (deciduous broadleaf forests), EBF (evergreen broadleaf forests), ENF (evergreen needleleaf forests), GRA (grasslands), OSH (open shrublands), and WET (wetlands). All pairwise hyperbolic relationships between GPP and SIF$_d$ were statistically significant with p<0.0001, except for IT-Cp2, Guy and FR-Mej sites. a and b denote the fitted parameters from the hyperbolic model.

Site name	R^2	a	b	RMSE	N	PFT
BE-Bra	0.64	16.15	0.37	1.92	288	MF
BE-Lcr	0.24	14.12	0.28	4.03	618	CRO
BE-Lon	0.37	79.75	4.36	6.16	572	CRO
BE-Vie	0.28	8.60	0.07	2.42	220	ENF
CH-Dav	0.21	4.87	0.05	1.76	350	ENF
CZ-BK1	0.34	12.23	0.04	3.62	160	ENF
CZ-Lnz	0.46	16.31	0.28	3.28	332	MF
CZ-Wet	0.28	13.11	0.31	3.66	292	WET
DE-Geb	0.56	19.49	0.63	3.44	236	CRO
DE-Gri	0.34	12.66	0.33	3.34	818	GRA
DE-Hai	0.57	21.80	1.12	2.94	802	DBF

Site name	R²	Slope	Intercept	RMSE	N	PFT
DE-HoH	0.43	19.63	0.67	4.36	944	DBF
DE-Hzd	0.50	16.20	0.63	2.87	248	DBF
DE-Kli	0.35	28.94	1.90	3.88	850	CRO
DE-RuR	0.22	11.02	0.15	3.88	274	GRA
DE-RuS	0.28	31.74	0.97	6.30	678	CRO
DE-RuW	0.10	8.94	0.02	2.62	216	ENF
DE-Tha	0.74	10.40	0.21	1.79	268	ENF
DK-Sor	0.87	74.20	3.51	2.71	298	DBF
FI-Hyy	0.36	9.14	0.13	2.54	498	ENF
FI-Sii	0.37	4.36	0.23	1.10	766	WET
FI-Var	0.12	4.83	0.02	2.08	560	ENF
FR-Aur	0.22	16.48	1.05	3.74	854	CRO
FR-Bil	0.19	8.02	0.07	3.32	836	ENF
FR-EM2	0.13	9.22	0.25	4.99	762	CRO
FR-Fon	0.75	23.71	0.77	2.72	932	DBF
FR-Hes	0.56	27.10	0.94	3.80	342	DBF
FR-LGt	0.44	11.10	0.40	2.22	1050	WET
FR-Mej	0.07	9.75	0.18	5.17	668	CRO
GF-Guy	0.012	12.36	0.02	2.65	774	EBF
IT-BCi	0.19	18.71	0.27	6.18	300	CRO
IT-Cp2	0.002	9.56	0.00	2.01	182	EBF
IT-Lsn	0.61	13.44	0.50	2.10	1510	OSH
IT-SR2	0.30	10.43	0.07	2.99	750	ENF
IT-Tor	0.50	11.99	0.25	2.91	566	GRA
NL-Loo	0.40	9.67	0.05	1.98	234	ENF
SE-Deg	0.42	2.16	0.18	0.55	602	WET
SE-Htm	0.35	9.91	0.10	2.91	808	ENF
SE-Nor	0.68	12.16	0.23	2.12	640	ENF
SE-Svb	0.18	7.00	0.03	2.70	900	ENF

Tab S4: Detailed results and statistics of the site-specific linear relationships between GPP and SIF_d. The sign $\pm$ denotes the 95% confidence interval on the slope and on the intercept for each relationship. R^2 denotes for the coefficient of determination. The units are for the slope in (gC m^{-2} d^{-1}/(mW m^{-2} sr^{-1} nm^{-1})), intercept in (gC m^{-2} d^{-1}), and RMSE (Root Mean Squared Error) in (gC m^{-2} d^{-1}). PFT represents the plant functional type of each site: MF (mixed forests), CRO (croplands), DBF (deciduous broadleaf forests), EBF (evergreen broadleaf forests), ENF (evergreen needleleaf forests), GRA (grasslands), OSH (open shrublands), and WET (wetlands). All pairwise linear relationships between GPP and SIF_d were statistically significant with $p<0.0001$, except for IT-Cp2 site ($p<0.604$).

Relatively moderate and strong relationships were found at DK-Sor, FR-Fon, BE-Bra, DE-Hai, DE-Tha, and IT-Lsn, which are DBF, MF, ENF and OSH vegetation type sites, respectively, with R^2 values being between 0.54 and 0.81 ($p<0.0001$). The weakest relationships were recorded at FI-Var, FR-EM2 and FR-Mej sites, and no significant relationship was found at GF-Guy and IT-Cp2.

Site name	R²	Slope	Intercept	RMSE	N	PFT
BE-Bra	0.59	11.27±1.07	3.33±0.45	2.00	300	MF
BE-Lcr	0.20	9.02±1.39	4.06±0.66	4.06	630	CRO
BE-Lon	0.27	12.33±1.64	2.1±0.89	6.05	582	CRO

BE-Vie	0.20	4.75±1.24	4.84±0.60	2.44	228	ENF
CH-Dav	0.15	4.17±0.96	2.67±0.26	1.74	406	ENF
CZ-BK1	0.35	18±3.62	5.92±0.79	3.38	178	ENF
CZ-Lnz	0.42	9.98±1.25	4.76±0.60	3.18	346	MF
CZ-Wet	0.20	9.46±2.16	3.12±0.71	3.68	306	WET
DE-Geb	0.53	10.04±1.18	2.12±0.68	3.80	254	CRO
DE-Gri	0.28	8.58±0.94	2.89±0.38	3.26	842	GRA
DE-Hai	0.57	9.23±0.54	1.40±0.32	2.91	852	DBF
DE-HoH	0.35	9.29±0.79	3.04±0.41	4.14	1002	DBF
DE-Hzd	0.41	8.56±1.25	2.40±0.57	2.73	260	DBF
DE-Kli	0.31	9.05±0.89	1.18±0.40	3.85	886	CRO
DE-RuR	0.17	6.87±1.76	4.59±0.87	3.80	280	GRA
DE-RuS	0.29	17.04±1.97	1.81±0.80	6.22	708	CRO
DE-RuW	0.16	5.02±1.51	6.42±0.57	2.61	230	ENF
DE-Tha	0.56	6.43±0.68	3.54±0.31	1.61	280	ENF
DK-Sor	0.81	14.06±0.77	2.09±0.56	2.73	310	DBF
FI-Hyy	0.27	8.05±1.10	3.33±0.34	2.68	554	ENF
FI-Sii	0.32	4.01±0.40	1.06±0.12	1.10	850	WET
FI-Var	0.13	4.73±0.92	3.23±0.20	2.00	690	ENF
FR-Aur	0.23	7.98±0.97	1.08±0.41	3.65	908	CRO
FR-Bil	0.17	6.47±0.95	3.98±0.32	3.13	884	ENF
FR-EM2	0.11	5.10±1.02	2.99±0.59	4.85	780	CRO
FR-Fon	0.66	11.91±0.53	2.48±0.27	2.71	986	DBF
FR-Hes	0.50	12.12±1.28	2.55±0.66	3.78	352	DBF
FR-LGt	0.43	8.02±0.55	1.76±0.22	2.29	1114	WET
FR-Mej	0.04	4.72±1.65	4.40±0.84	5.22	672	CRO
GF-Guy	0.02	1.86±0.91	10.79±0.57	2.63	774	EBF
IT-BCi	0.16	13.43±3.5	5.10±1.39	6.11	306	CRO
IT-Cp2	0.001	0.36±1.37	9.37±0.54	2.01	190	EBF
IT-Lsn	0.54	8±0.36	2.17±0.17	2.10	1594	OSH
IT-SR2	0.21	6.78±0.94	5.78±0.36	2.95	774	ENF
IT-Tor	0.42	11.31±1.02	2.30±0.30	2.83	646	GRA
NL-Loo	0.24	5.36±1.22	5.96±0.48	2.19	242	ENF
SE-Deg	0.35	2.04±0.21	0.61±0.06	0.54	680	WET
SE-Htm	0.29	6.34±0.66	4.70±0.30	2.72	860	ENF
SE-Nor	0.51	8.35±0.62	3.53±0.25	2.14	684	ENF
SE-Svb	0.20	7.61±0.93	3.88±0.24	2.75	1056	ENF

Table 5: Summary statistics of plant functional type-specific linear relationship between GPP and SIF_d in eight major PFT. All pairwise linear relationships between GPP and SIF_d were statistically significant with $p<0.0001$. The units are for the slope in (gC m^{-2} d^{-1}/ (mW m^{-2} sr^{-1} nm^{-1})), intercept in (gC m^{-2} d^{-1}), and RMSE in (gC m^{-2} d^{-1}). The sign ± denotes the 95% confidence interval on the slope and intercept of the relationships between SIF_d and GPP. Relatively moderate and goodness of fits were found in MF, DBF and OSH biomes, and the lowest in EBF and CRO vegetation types.

PFT	Sites	R^2	Slope	Intercept	RMSE	N
CRO	9	0.18	8.93±0.49	2.61±0.24	5.24	5726

DBF	6	0.52	10.75±0.33	2.32±0.18	3.50	3762
EBF	2	0.07	3.08±0.72	9.76±0.42	2.62	964
ENF	13	0.26	7.28±0.28	4.07±0.10	2.85	7066
GRA	3	0.33	9.39±0.62	2.79±0.24	3.24	1768
MF	2	0.47	10.53±0.87	4.10±0.39	2.74	646
OSH	1	0.54	8.00±0.36	2.17±0.17	2.10	1594
WET	4	0.29	7.14±0.40	1.15±0.14	2.44	2950
ALL	40	0.30	9.12±0.17	2.87±0.08	3.82	24476

Tab S6: The generalized linear model results statistics (GLM). The following equation was fitted to investigate the effects of the site, year, and PFT and their interactions on the seasonal and interannual variations of SIF_d and its relationship with GPP. $SIF_d = 1 + Year + Site + PFT + GPP + Year \times GPP + Site \times GPP + PFT \times GPP$. All pairwise relationships between GPP and SIF_d were statistically significant with $p<0.001$, except for Site×GPP interaction ($p<0.896$).

Parameters	Estimate	Std. Error	p-value
Intercept	-3.01E+01	5.79E+00	2.00E-07
Year	1.50E-02	2.87E-03	1.66E-07
Site	-1.06E-03	2.49E-04	2.13E-05
PFT	-1.31E-02	1.02E-03	< 2e-16
GPP	3.09E+00	7.60E-01	4.83E-05
Year×GPP	-1.52E-03	3.76E-04	5.70E-05
Site×GPP	-4.17E-06	3.19E-05	0.896
PFT×GPP	1.88E-03	1.59E-04	< 2e-16

Tab S7: Detailed results and statistics of the site-specific comparison between tower-based observed GPP against the RF predicted GPP. PFT denotes plant functional type of each site, including MF (mixed forests), CRO (croplands), DBF (deciduous broadleaf forests), EBF (evergreen broadleaf forests), ENF (evergreen needleleaf forests), GRA (grasslands), OSH (open shrublands), and WET (wetlands). The adj. R^2 denotes for the adjusted coefficient of determination. The units are for the slope in (gC m^{-2} d^{-1}/(mW m^{-2} sr^{-1} nm^{-1})), intercept in (gC m^{-2} d^{-1}), and RMSE (Root Mean Squared Error) in (gC m^{-2} d^{-1}). The sign ± denotes the confidence interval at 95% probability level on the slope and on the intercept for each relationship. RF-R model includes only surface spectral reflectance as explanatory variables, RF-SIF-R uses SIF_d and spectral bands inputs to predict GPP, RF-SIF-VI explores SIF_d and VIs as inputs, and RF-SIF-PFT establishes based on SIF_d, spectral bands and vegetation type as categorial variable to estimate GPP.

					RF-R				RF-SIF-R	
Site name	PFT	N	adj. R^2	Slope	Intercept	RMSE	adj. R^2	Slope	Intercept	RMSE
BE-Bra	MF	55	0.62	0.84±0.18	1.29±1.43	1.70	0.71	0.98±0.17	0.15±1.37	1.49
BE-Lcr	CRO	124	0.92	1.03±0.05	-0.14±0.47	1.26	0.9	1.06±0.06	-0.39±0.54	1.40
BE-Lon	CRO	111	0.91	1.03±0.06	-0.24±0.55	1.93	0.88	1.09±0.07	-0.45±0.65	2.22
BE-Vie	ENF	41	0.81	1.02±0.16	-0.07±1.04	1.08	0.70	1.00±0.21	-0.20±1.43	1.37
CH-Dav	ENF	95	0.84	0.95±0.09	-0.01±0.34	0.79	0.75	0.87±0.10	0.04±0.43	0.98
CZ-BK1	ENF	23	0.63	0.96±0.32	0.86±3.03	2.28	0.70	1.31±0.37	-1.22±3.16	2.04
CZ-Lnz	MF	62	0.93	1.13±0.08	-0.81±0.78	1.12	0.87	1.15±0.12	-0.67±1.08	1.53
CZ-Wet	WET	54	0.88	0.98±0.10	-0.02±0.74	1.48	0.79	1.09±0.16	-0.52±1.09	1.97
DE-Geb	CRO	48	0.83	1.06±0.14	-0.14±1.11	2.23	0.87	1.05±0.12	0.11±0.93	1.95
DE-Gri	GRA	169	0.81	1.09±0.08	-0.49±0.52	1.58	0.77	1.12±0.09	-0.61±0.60	1.74
DE-Hai	DBF	161	0.90	1.01±0.05	-0.26±0.38	1.46	0.87	1.01±0.06	-0.57±0.46	1.66
DE-HoH	DBF	183	0.94	1.00±0.04	-0.06±0.33	1.28	0.90	1.04±0.05	-0.29±0.43	1.61

Site name	PFT	N	adj. R²	Slope	Intercept	RMSE	adj. R²	Slope	Intercept	RMSE
DE-Hzd	DBF	61	0.84	1.03±0.12	0.02±0.74	1.43	0.84	1.14±0.13	-0.83±0.83	1.44
DE-Kli	CRO	177	0.88	1.02±0.06	-0.58±0.35	1.59	0.83	1.08±0.07	-1.12±0.47	1.93
DE-RuR	GRA	61	0.75	0.95±0.14	0.66±1.14	1.82	0.59	1.05±0.23	0.19±1.71	2.33
DE-RuS	CRO	148	0.79	0.98±0.08	0.68±0.77	3.13	0.74	0.98±0.09	0.82±0.87	3.50
DE-RuW	ENF	46	0.81	0.96±0.14	0.38±1.13	1.14	0.54	0.94±0.26	0.78±2.03	1.78
DE-Tha	ENF	52	0.77	0.93±0.14	0.61±0.90	1.14	0.67	0.85±0.17	0.85±1.10	1.38
DK-Sor	DBF	59	0.94	1.05±0.07	0.15±0.88	1.56	0.93	1.04±0.08	0.39±0.96	1.73
FI-Hyy	ENF	104	0.92	1.02±0.06	-0.15±0.37	0.91	0.81	1.05±0.10	-0.23±0.61	1.41
FI-Sii	WET	163	0.86	0.91±0.06	0.01±0.15	0.49	0.69	0.68±0.08	0.30±0.21	0.72
FI-Var	ENF	139	0.79	0.97±0.08	0.13±0.38	1.05	0.74	0.96±0.10	0.12±0.43	1.16
FR-Aur	CRO	205	0.86	1.00±0.06	-0.14±0.28	1.45	0.83	1.00±0.06	-0.10±0.32	1.61
FR-Bil	ENF	168	0.89	1.05±0.06	-0.13±0.35	1.15	0.82	1.09±0.08	-0.35±0.48	1.48
FR-EM2	CRO	169	0.62	0.94±0.11	0.62±0.75	2.97	0.59	0.86±0.11	1.03±0.74	3.08
FR-Fon	DBF	210	0.95	1.01±0.03	-0.20±0.25	0.97	0.95	1.02±0.03	-0.34±0.28	1.06
FR-Hes	DBF	74	0.83	1.00±0.10	-0.70±0.98	2.07	0.80	1.08±0.12	-1.43±1.14	2.24
FR-LGt	WET	239	0.93	1.03±0.04	-0.34±0.19	0.82	0.85	1.01±0.05	-0.45±0.28	1.15
FR-Mej	CRO	120	0.81	0.98±0.09	0.21±0.74	2.44	0.74	1.09±0.12	-0.34±0.95	2.89
GF-Guy	EBF	146	0.80	0.99±0.53	0.21±0.96	1.18	0.71	1.00±0.10	0.35±1.20	1.42
IT-BCi	CRO	69	0.21	1.16±0.53	0.94±5.08	5.98	0.21	0.61±0.28	5.31±3.23	5.98
IT-Cp2	EBF	42	0.36	0.65±0.27	3.89±2.51	1.25	0.25	0.58±0.31	4.85±2.73	1.36
IT-Lsn	OSH	317	0.91	1.02±0.04	-0.09±0.22	0.99	0.88	1.01±0.04	0.01±0.24	1.10
IT-SR2	ENF	160	0.60	0.96±0.12	0.55±1.02	2.04	0.56	1.08±0.15	-0.08±1.18	2.12
IT-Tor	GRA	134	0.79	0.97±0.09	0.19±0.43	1.60	0.75	1.00±0.10	0.13±0.49	1.74
NL-Loo	ENF	47	0.77	1.11±0.18	-0.46±1.32	1.30	0.66	1.19±0.25	-0.55±1.73	1.58
SE-Deg	WET	143	0.38	0.37±0.08	0.56±0.13	0.53	0.41	0.34±0.07	0.49±0.14	0.52
SE-Htm	ENF	167	0.78	1.02±0.08	-0.03±0.63	1.52	0.70	1.04±0.10	-0.17±0.78	1.77
SE-Nor	ENF	144	0.87	0.97±0.06	0.15±0.41	1.05	0.79	0.99±0.09	0.16±0.55	1.33
SE-Svb	ENF	199	0.92	1.01±0.04	0.00±0.02	0.91	0.86	1.05±0.06	-0.21±0.34	1.15

Site name	PFT	N	**RF-SIF-VI**				**RF-SIF-R-PFT**			
			adj. R²	Slope	Intercept	RMSE	adj. R²	Slope	Intercept	RMSE
BE-Bra	MF	55	0.59	0.85±0.19	1.18±1.53	1.76	0.72	0.97±0.16	0.14±1.34	1.47
BE-Lcr	CRO	124	0.85	1.08±0.08	-0.13±0.68	1.77	0.91	1.05±0.06	-0.33±0.53	1.39
BE-Lon	CRO	111	0.83	1.12±0.10	-0.54±0.82	2.72	0.88	1.08±0.07	-0.36±0.65	2.22
BE-Vie	ENF	41	0.67	0.95±0.21	0.13±1.45	1.42	0.75	1.05±0.19	-0.61±1.32	1.23
CH-Dav	ENF	95	0.71	0.85±0.11	0.16±0.46	1.05	0.76	0.88±0.10	0.02±0.42	0.96
CZ-BK1	ENF	23	0.40	1.04±0.55	1.68±4.24	2.90	0.67	1.30±0.40	-1.21±3.40	2.15
CZ-Lnz	MF	62	0.75	1.11±0.16	-0.34±1.54	2.11	0.86	1.16±0.12	-0.90±1.12	1.55
CZ-Wet	WET	54	0.68	1.13±0.21	-0.59±1.42	2.42	0.82	1.11±0.14	-0.34±0.96	1.81
DE-Geb	CRO	48	0.8	0.99±0.14	0.31±1.15	2.40	0.87	1.05±0.12	0.15±0.92	1.92
DE-Gri	GRA	169	0.65	1.03±0.12	-0.37±0.77	2.16	0.78	1.13±0.09	-0.84±0.59	1.69
DE-Hai	DBF	161	0.82	0.99±0.07	-0.72±0.54	1.91	0.88	1.02±0.06	-0.48±0.43	1.58
DE-HoH	DBF	183	0.87	1.09±0.06	-0.52±0.52	1.88	0.90	1.03±0.05	-0.17±0.43	1.61
DE-Hzd	DBF	61	0.74	1.07±0.16	-0.67±1.06	1.81	0.86	1.09±0.11	-0.34±0.71	1.34
DE-Kli	CRO	177	0.71	1.03±0.10	-1.15±0.63	2.49	0.84	1.07±0.07	-1.07±0.44	1.84
DE-RuR	GRA	61	0.57	0.97±0.22	-0.01±1.81	2.37	0.60	1.07±0.22	0.02±1.69	2.28
DE-RuS	CRO	148	0.72	1.05±0.11	0.77±0.91	3.62	0.75	0.98±0.09	0.84±0.85	3.45
DE-RuW	ENF	46	0.35	0.74±0.30	2.53±2.24	2.12	0.56	0.97±0.26	0.54±2.00	1.74

DE-Tha	ENF	52	0.54	0.74±0.19	1.32±1.31	1.63	0.69	0.93±0.18	0.34±1.16	1.35
DK-Sor	DBF	59	0.90	1.06±0.09	0.58±1.10	1.98	0.93	1.04±0.08	0.34±0.95	1.71
FI-Hyy	ENF	104	0.74	1.06±0.12	-0.17±0.73	1.65	0.81	1.06±0.10	-0.35±0.62	1.41
FI-Sii	WET	163	0.68	0.64±0.07	0.27±0.21	0.73	0.78	0.89±0.07	0.10±0.18	0.60
FI-Var	ENF	139	0.66	0.90±0.11	0.28±0.50	1.32	0.73	0.94±0.10	0.14±0.44	1.18
FR-Aur	CRO	205	0.79	0.99±0.07	-0.18±0.36	1.80	0.83	0.99±0.06	-0.06±0.32	1.62
FR-Bil	ENF	168	0.71	1.05±0.10	-0.05±0.62	1.87	0.82	1.10±0.08	-0.57±0.49	1.47
FR-EM2	CRO	169	0.55	0.85±0.12	1.09±0.80	3.25	0.60	0.86±0.11	1.05±0.74	3.07
FR-Fon	DBF	210	0.87	1.00±0.05	-0.22±0.44	1.63	0.95	1.02±0.03	-0.29±0.27	1.03
FR-Hes	DBF	74	0.60	1.01±0.19	-0.87±1.72	3.18	0.81	1.07±0.12	-1.24±1.12	2.22
FR-LGt	WET	239	0.74	0.90±0.07	-0.38±0.40	1.53	0.88	1.06±0.05	-0.39±0.25	1.05
FR-Mej	CRO	120	0.68	1.07±0.13	-0.37±1.09	3.20	0.75	1.08±0.11	-0.28±0.92	2.81
GF-Guy	EBF	146	0.53	0.89±0.14	2.07±1.51	1.81	0.75	1.05±0.10	-0.36±1.17	1.33
IT-BCi	CRO	69	0.21	0.63±0.29	5.16±3.33	6.00	0.20	0.60±0.28	5.46±3.24	6.02
IT-Cp2	EBF	42	0.10	0.35±0.29	7.13±2.42	1.49	0.3	0.65±0.31	3.95±2.84	1.31
IT-Lsn	OSH	317	0.83	0.98±0.05	0.21±0.29	1.33	0.89	1.02±0.04	-0.06±0.24	1.08
IT-SR2	ENF	160	0.38	1.02±0.20	0.80±1.51	2.52	0.58	1.11±0.15	-0.34±1.16	2.07
IT-Tor	GRA	134	0.71	0.98±0.11	0.19±0.53	1.88	0.75	0.99±0.10	0.08±0.49	1.74
NL-Loo	ENF	47	0.47	1.05±0.33	0.61±2.14	1.96	0.69	1.22±0.24	-0.98±1.70	1.51
SE-Deg	WET	143	0.38	0.22±0.05	0.54±0.14	0.53	0.55	0.50±0.07	0.34±0.13	0.45
SE-Htm	ENF	167	0.56	0.98±0.13	0.27±0.99	2.15	0.72	1.08±0.10	-0.44±0.77	1.71
SE-Nor	ENF	144	0.70	0.94±0.10	0.61±0.63	1.57	0.81	1.02±0.08	-0.14±0.52	1.24
SE-Svb	ENF	199	0.68	0.99±0.09	0.16±0.55	1.76	0.87	1.04±0.06	-0.26±0.35	1.15

Figure S1: Site-specific linear relationships tower-based GPP and SIF_d at daily timescale. The R^2 represents the coefficient of determination of the relationship between GPP and SIF_d for each site. The color code represents the eight different plant functional types encountered in the study sites: Red color stands for CRO (croplands), green for DBF (deciduous broadleaf forests), yellow for EBF (evergreen broadleaf forests), magenta for ENF (evergreen needleleaf forests), blue for GRA (grasslands), Cyan for MF (mixed forests), lime for OSH (open shrubland), and dimgrey for WET (wetland). The shaded area depicted in each line is the 95% confidence interval of the linear relationship between GPP and SIF_d.
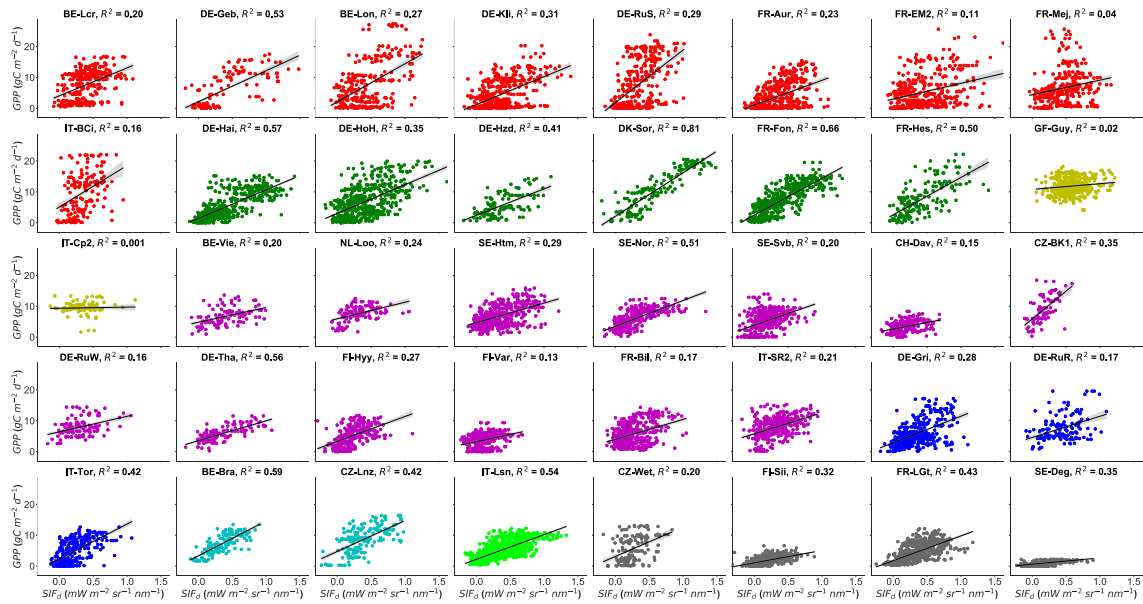
Figure S2: linear relationships between tower-based GPP and SIF_d in eight plant functional types: MF, CRO, ENF, DBF, EBF, GRA, OSH, and WET at daily timescale. The R^2 represents the coefficient of determination of the relationship between GPP and SIF_d. p is the probability value of the linear model. The shaded area depicted in each line is the 95% confidence interval of the linear relationships between GPP and SIF_d.
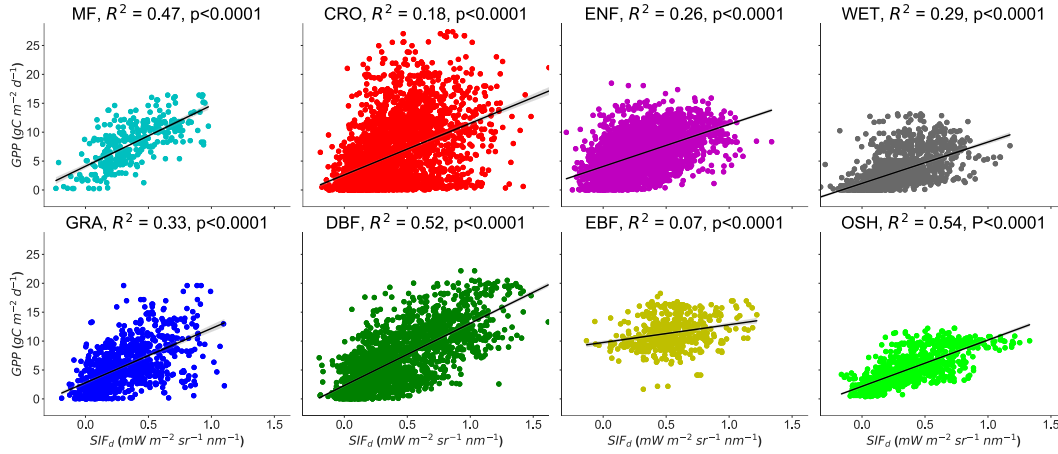
Figure S3: Scatterplots of the linear relationships between tower-based GPP and SIF_d in eight PFT pooled together across all sites. The shaded area depicted in each line is the 95% confidence interval of the linear relationships between GPP and SIF_d.
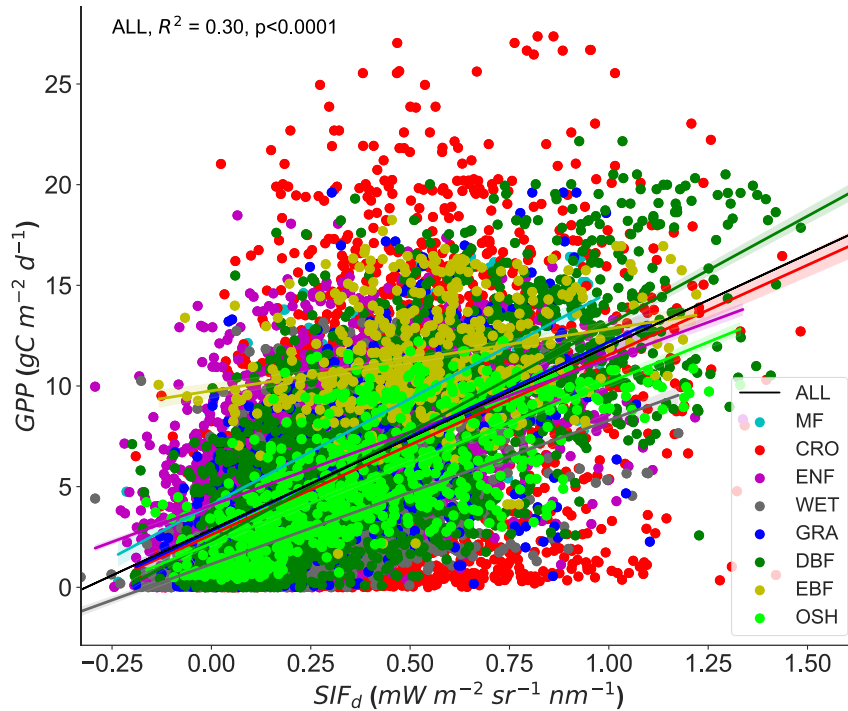
Figure S4: Correlation matrix between variables. B_1 to B_{16} denote the spectral reflectance of MODIS bands, SIF_d is the daily TROPOMI sun-induced chlorophyll fluorescence, GPP is the tower-based daily gross primary production, NDVI (normalized difference vegetation index), NIRv (near infrared reflectance of vegetation index), and PRI (photochemical reflectance index). The correlation matrix shows strong relations between variables. Based on these observations B_{10}, B_{12} and B_{14} were excluded from the explanatory variables for establishing the RF regression models. Furthermore, B_{15} and B_{16} were excluded from the analyses due to many missing values that they contained.
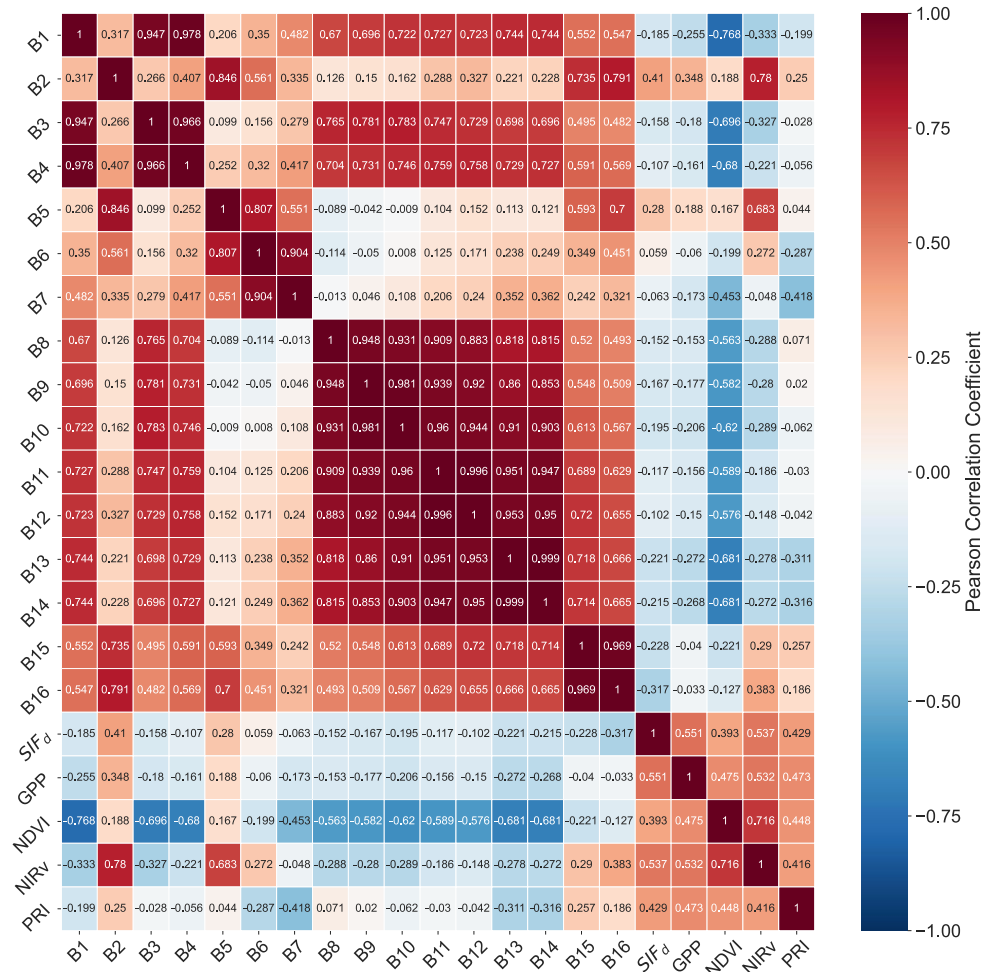
Figure S5: Comparison between RF models estimated GPP and observed tower-based GPP across all ICOS flux tower sites. Overall, our RF models show a high explanation of GPP variability across different vegetation types. However, the RF-SIF-VI shows some limits in some sites in predicting tower-based GPP as it overestimates (for instance at *SE-Deg*) and underestimates (for instance at *IT-Cp2*) tower-based GPP. The color code represents the different RF GPP predictions and the observed GPP: Red color stands for RF-SIF-R, green for RF-SIF-R-PFT, blue for RF-R, Cyan for RF-SIF-VI, and black for the observed tower-based GPP.
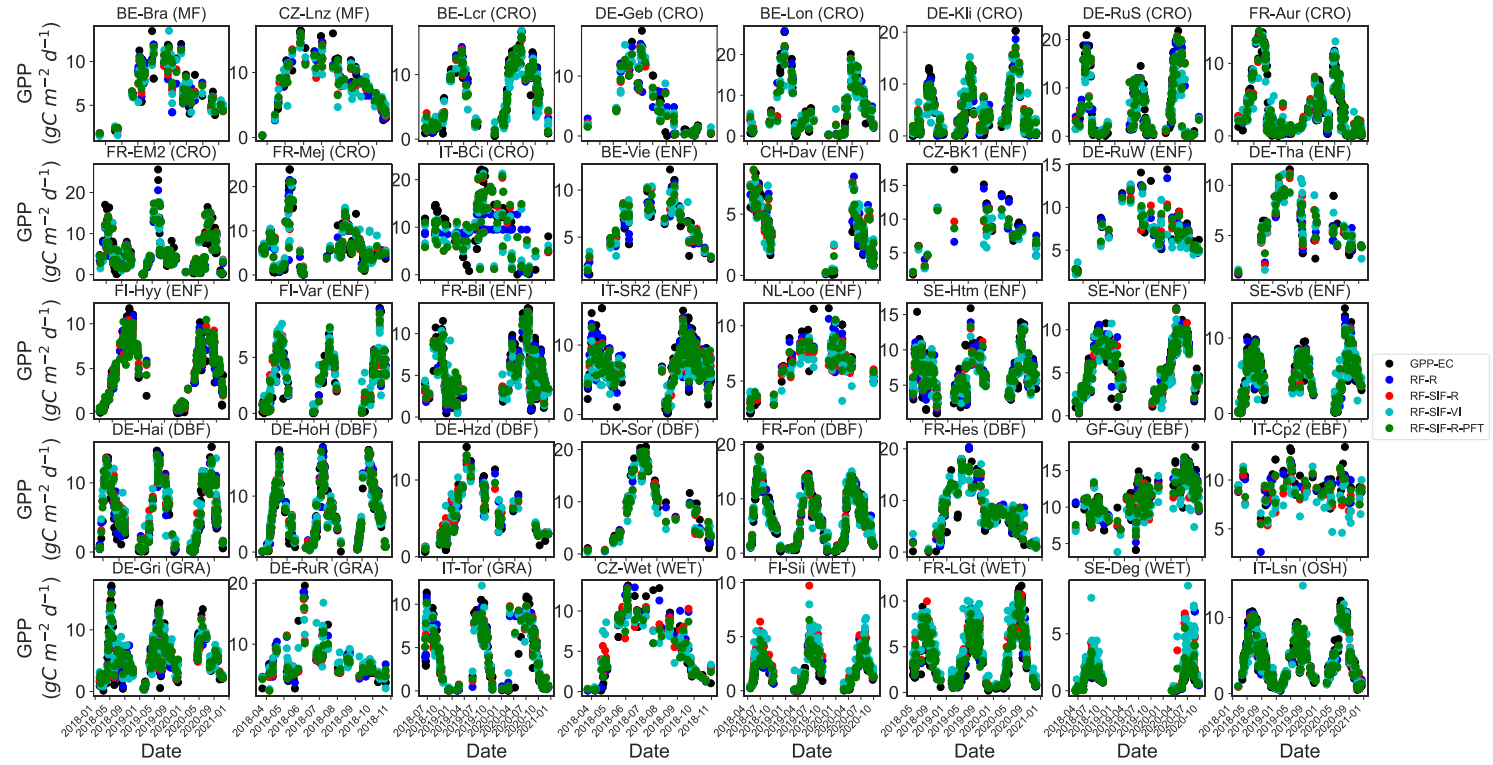
Figure S6-a RF-R: Scatterplots between tower-based GPP and RF-R predicted GPP of each site. The adj. R² represents the adjusted coefficient of determination of the relationships between observed GPP and predicted GPP. The color code represents the eight different plant functional types encountered in the study sites: Red color stands for CRO (croplands), green for DBF (deciduous broadleaf forests), yellow for EBF (evergreen broadleaf forests), magenta for ENF (evergreen needleleaf forests), blue for GRA (grasslands), Cyan for MF (mixed forests), lime for OSH (open shrubland), and dimgrey for WET (wetland). The shaded area depicted in each line is the 95% confidence interval of the relationships between predicted GPP and observed GPP.
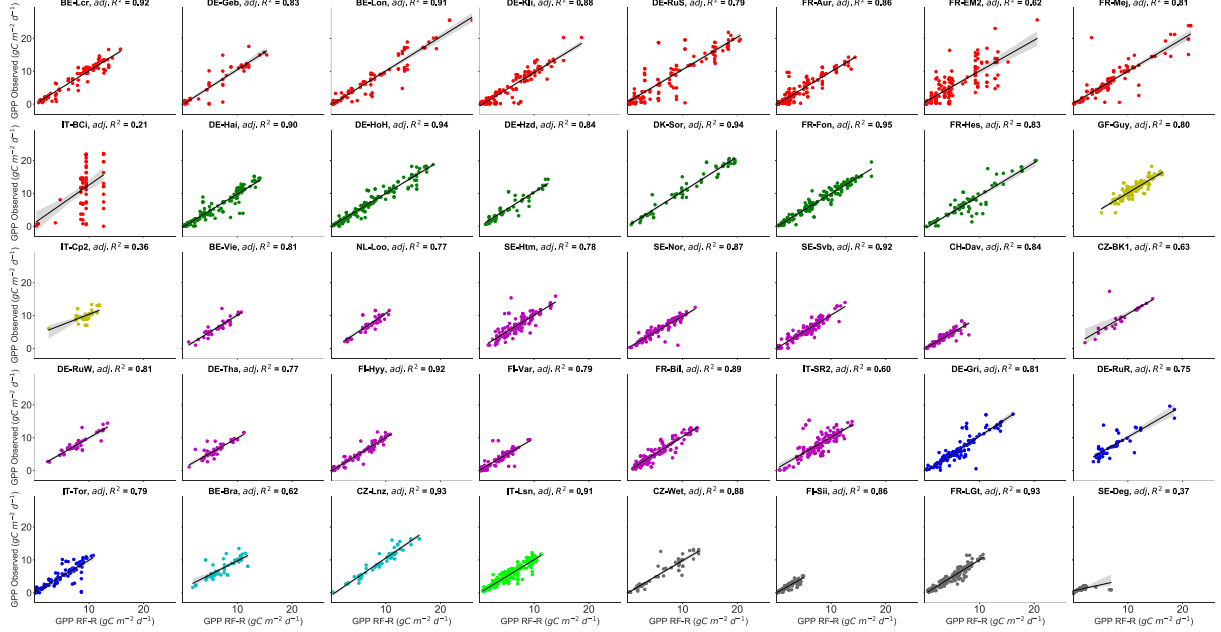
Figure S6-b RF-R: Scatterplots of the tower-based GPP against RF-R predicted GPP based on each PFT: mixed forests (MF), croplands (CRO), evergreen needleleaf forests (ENF), deciduous broadleaf forests (DBF), evergreen broadleaf forests (EBF), grasslands (GRA), open shrublands (OSH), and wetlands (WET) at daily timescale. The adj. R² represents the adjusted coefficient of determination of the relationship between observed GPP and predicted GPP. p denotes the statistically significant level of the relationships. The shaded area depicted in each line is the 95% confidence interval of the relationships between predicted GPP and observed GPP.
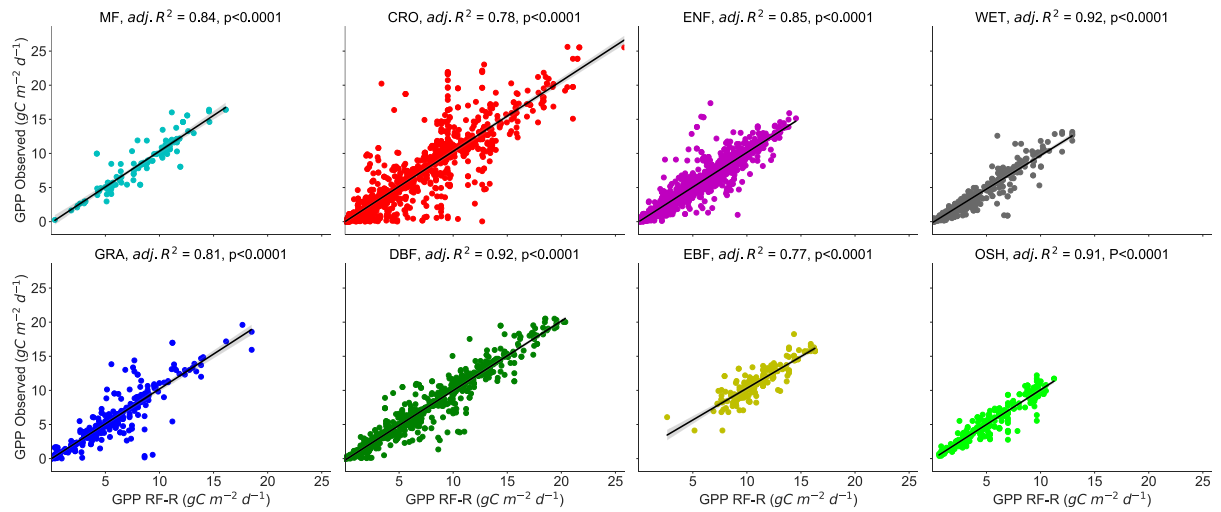
Figure S7-a RF-SIF-VI: Scatterplots between tower-based GPP and RF-SIF-VI predicted GPP for each site. The adj. R² represents the adjusted coefficient of determination of the relationships between observed GPP and predicted GPP. The color code represents the eight different vegetation types encountered in the study sites: Red color stands for CRO (croplands), green

for DBF (deciduous broadleaf forests), yellow for EBF (evergreen broadleaf forests), magenta for ENF (evergreen needleleaf forests), blue for GRA (grasslands), Cyan for MF (mixed forests), lime for OSH (open shrubland), and dimgrey for WET (wetland). The shaded area depicted in each line is the 95% confidence interval of the relationships between predicted GPP and observed GPP.
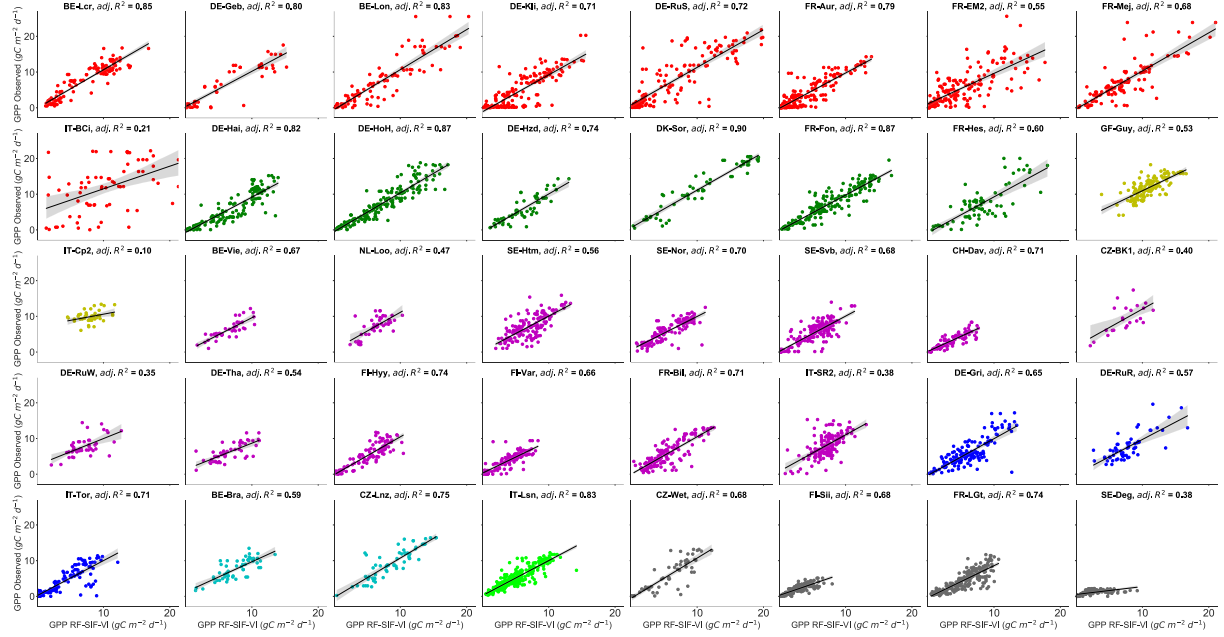
Figure S7-b RF-SIF-VI: Scatterplots of the tower-based GPP against RF-SIF-VI predicted GPP for each plant functional types: mixed forests (MF), croplands (CRO), evergreen needleleaf forests (ENF), deciduous broadleaf forests (DBF), evergreen broadleaf forests (EBF), grasslands (GRA), open shrublands (OSH), and wetlands (WET) at daily timescale. The adj. R^2 represents the adjusted coefficient of determination of the relationship between observed GPP and predicted GPP. p denotes the statistically significant level of the relationships. The shaded area depicted in each line is the 95% confidence interval of the relationships between predicted GPP and observed GPP. The strongest correlations between observed and predicted GPP are observed in DBF and OSH vegetation types, while the lowest are recorded in EBF and ENF.
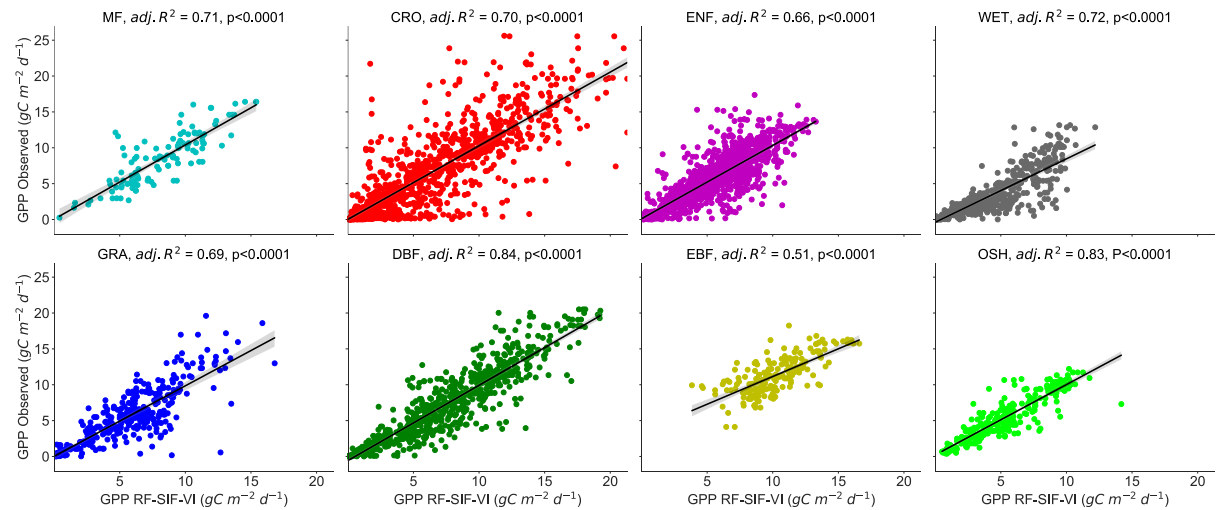
Figure S8-a RF-SIF-R-PFT: Scatterplots between tower-based GPP and RF-SIF-R-PFT predicted GPP for each site. The adj. R^2 represents the adjusted coefficient of determination of the agreement between predicted GPP and observed GPP. The color code represents the eight different vegetation types encountered in the study sites: Red color stands for CRO (croplands), green

for DBF (deciduous broadleaf forests), yellow for EBF (evergreen broadleaf forests), magenta for ENF (evergreen needleleaf forests), blue for GRA (grasslands), Cyan for MF (mixed forests), lime for OSH (open shrubland), and dimgrey for WET (wetland). The shaded area depicted in each line is the 95% confidence interval of relationships between predicted GPP and observed GPP.
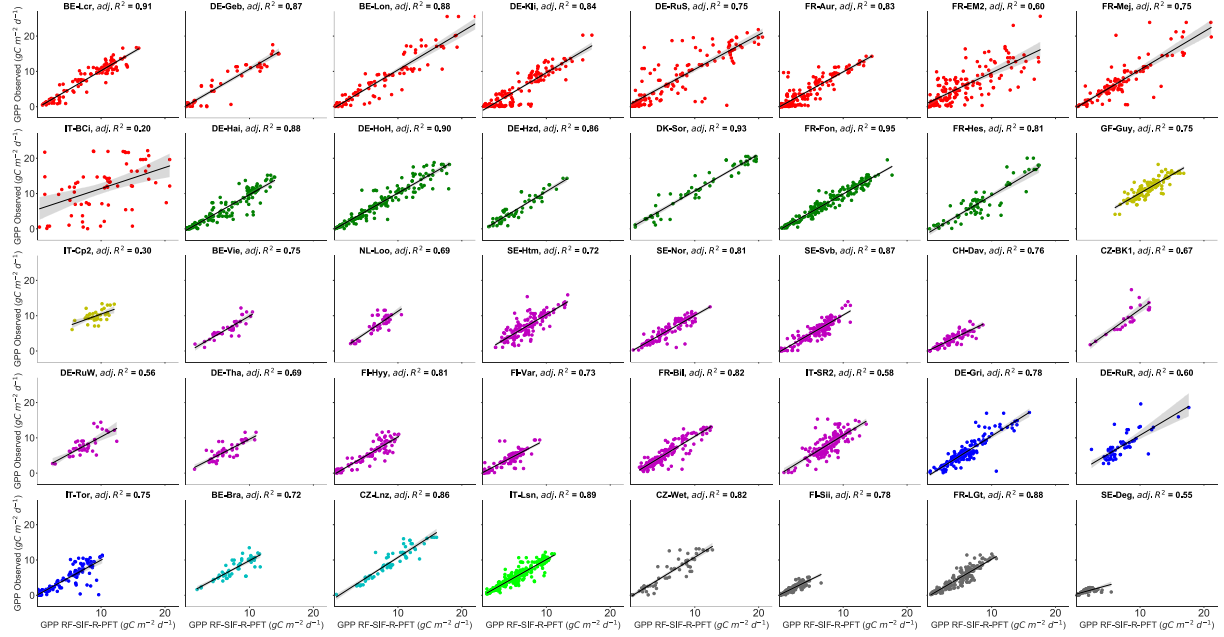
Figure S8-b RF-SIF-R-PFT: Scatterplots of the ICOS tower-based GPP against RF-SIF-R-PFT predicted GPP for each plant functional type: mixed forests (MF), croplands (CRO), evergreen needleleaf forests (ENF), deciduous broadleaf forests (DBF), evergreen broadleaf forests (EBF), grasslands (GRA), open shrublands (OSH), and wetlands (WET) at daily timescale. The adj. R^2 represents the adjusted coefficient of determination of the relationship between observed GPP and predicted GPP. p denotes the statistically significant level of the relationships. The shaded area depicted in each line is the 95% confidence interval of the relationships between GPP predicted and GPP observed.